

Magnetic Field Dependence of Optical  
Coherence Times in Quantum Computer  
Hardware Based on  $\text{Pr}^{3+}:\text{Y}_2\text{SiO}_5$

Master Thesis

by

Magnus Trägårdh

Lund Reports on Atomic Physics, LRAP-366

Lund, July 2006



### **Abstract**

This thesis investigates how the coherence time of the  ${}^3\text{H}_4 - {}^1\text{D}_2$  transition of praseodymium doped into a YSO crystal is affected by an externally applied magnetic field. Such crystals, kept at or below helium temperature, are considered for use as hardware in a future quantum computer, and the coherence time is one important factor affecting the error rate of gate operations in this computer. If the coherence time could be increased by magnetic fields, it could increase the fidelity of gate operations, bringing it closer to values where quantum computing becomes viable.

The measurements were made using two-pulse photon echoes, and the measured coherence times were determined to approximately  $60 \mu\text{s}$ , which corresponds to a homogeneous linewidth of 5 kHz. The coherence times showed no clear magnetic field dependence and were substantially shorter than previously reported. It could not be determined whether this was the result of unforeseen processes destroying the coherence or due to an experimental artifact.

In addition, the report contains instructions and advice for operating the Photon Echo Group's Oxford Instruments Spectromag cryostat and superconducting magnet system, since it was mainly the author's responsibility to put this system into operation.



# Populärvetenskaplig sammanfattning

Utvecklingentakten för datorer har varit explosionsartad de senaste årtiondena. I sin strävan att göra datorerna allt kraftfullare bygger tillverkarna kretsar för morgondagens datorer som innehåller fler elektroniska komponenter än vad motsvarande kretsar för dagens datorer gör. Därför blir komponenterna allt mindre och kommer inom en överskådlig framtid att ha storlekar som är jämförbara med enstaka atomer.

När man kommer ner på atomnivå möts man av en värld som är mycket anorlunda den vi känner från vår vanliga, makroskopiska tillvaro. Här gäller inte de klassiska rörelselagarna som formulerades av Newton på 1600-talet. Istället tillämpas *kvantmekanik*, en teori som utarbetades i början av 1900-talet av storheter som Max Planck, Erwin Schrödinger och Werner Heisenberg. Kvantmekaniken är en av de mest framgångsrika vetenskapliga teorier som någonsin funnits i den meningen att den visat sig kunna förutsäga resultaten av experiment med en oerhörd noggrannhet, men den innehåller många fenomen som står i strid med vardagsförnuftet: System som i någon mening befinner sig i flera tillstånd samtidigt, partiklar som går flera vägar samtidigt och inte bestämmer sig för var de egentligen är förrän en forskare "tvingar" dem att bestämma sig genom att mäta var de egentligen finns, partiklar som påverkar varandra över långa avstånd utan att det egentligen verkar några krafter mellan dem, för att de har interagerat någon gång i det förflutna ...

Datorindustrin måste alltså i framtiden ta mer och mer hänsyn till kvantmekaniska fenomen. Intressant nog visar det sig att kvantmekaniska fenomen kan användas för att bygga kraftfulla datorer som kan lösa vissa problem långt mer effektivt än en vanlig klassisk dator skulle kunna göra. En sådan dator använder just sådana fenomen som att ett kvantmekaniskt system kan vara i flera tillstånd samtidigt (*superposition, kvantparallellism*) och att en kvantmekanisk partikel kan påverka andra partiklar som den interagerat med tidigare (*sammanflätning, eng. entanglement*). Framför allt är man intresserad av kvantdatorernas förmåga att söka i databaser och att dela upp stora tal i primtalsfaktorer. Det senare är intressant framför allt för att många moderna kryptosystem som används för säker kommunikation bland annat på internet, till exempel överföringar av kortnummer vid betalningar, grundar sig på det faktum att det är svårt att faktorisera stora tal i primtalsfaktorer.

Men även om kvantdatorer i teorin är kraftfullare än klassiska datorer så har

det visat sig vara mycket svårt att bygga dem i verkligheten. Precis som klassisk information kan representeras på olika sätt, till exempel som magnetisering på en hårddisk eller ljuspulser i en fiberkabel, så kan informationen i en kvantdator representeras på många olika sätt. Därför finns det en uppsjö av koncept för hur en kvantdator rent praktiskt skall se ut och fungera. Inget av dem har nått några stora framgångar än så länge. Ett stort problem är att de kvantmekaniska tillstånden som representerar information i datorn är mycket känsliga för störningar. Informationen i en klassisk dator existerar som bitar, som kan vara antingen i tillståndet 0 eller 1. Kvantinformation lagras däremot i kvanttillstånd som kan vara i en kombination (*superposition*) av 0 och 1, och dessa tillstånd är mycket ömtåliga.

Fotonekogrupper vid Avdelningen för Atomfysik, Lunds Tekniska Högskola, arbetar på ett koncept som går ut på att bygga en kvantdator baserad på en genomskinlig kristall, där man har tillsatt små mängder av en sällsynt jordartsmetall. För att lagra information utnyttjar man att atomer bara kan ha vissa kvantmekaniska tillstånd med bestämda energier. Ett visst energitillstånd för de sällsynta jordartsatomerna betyder då en 0:a, och ett annat tillstånd betyder en 1:a. Beräkningar utförs genom att man skickar laserpulser på atomerna.

Det här konceptet har, precis som alla andra kvantdatorkoncept, många problem att lösa innan det blir en fungerande dator. Som nämnts är kvanttillstånden mycket känsliga, och de minsta störningar kan få atomerna att "glömma" den information som de skall representera. Vid rumstemperatur är det vibrationer i kristallen som är det största problemet. Detta kan dock avhjälpas genom att kyla ner kristallen till temperaturer bara ett par grader över den absoluta nollpunkten,  $-273^{\circ}\text{C}$ . Detta görs i så kallade *kryostat*er, där kristallen kyls ned med hjälp av flytande kväve ( $-196^{\circ}\text{C}$ ) och flytande helium ( $-269^{\circ}\text{C}$ ). Tyvärr återstår fler problem: Både de sällsynta jordartsmetallernas atomkärnor och kristallens atomkärnor fungerar som små magneter, som ligger och vrider sig fram och tillbaka. Detta ger magnetiska störningar som förstör kvanttillstånden.

Syftet med examensarbetet har varit att undersöka hur tiden som ett kvanttillstånd kan bevaras, den så kallade *koherenstiden*, påverkas av att man lägger på ett yttre magnetfält. Undersökningarna har gjorts för den kristall som för närvarande är huvudkandidaten för kvantdatorhårdvara, praseodymdopad yttriumsilikat ( $\text{Pr}^{3+}:\text{Y}_2\text{SiO}_5$ ). Det pålagda fältet tvingar förhoppningsvis atomkärnorna att ställa in sig i ett visst läge och hindrar dem från att vrida sig. Genom att skicka in lämpliga laserpulser i kristallen kan man få den att själv skicka ut en ljuspuls, ett så kallat fotoneko. Storleken på fotonekot ger information om hur lång koherenstiden är. Tyvärr kunde experimentet inte visa att magnetfältet gjorde någon skillnad: Koherenstiden var ungefär  $60 \mu\text{s}$  avsett om det fanns något magnetfält eller inte.

# Contents

<b>1</b>	<b>Introduction</b>	<b>7</b>
1.1	Background . . . . .	7
1.2	Goal . . . . .	8
1.3	Outline . . . . .	8
<b>2</b>	<b>Quantum Computing</b>	<b>9</b>
2.1	History of Quantum Computing . . . . .	9
2.2	Qubits and Quantum Registers . . . . .	9
2.3	Quantum Gates . . . . .	10
2.4	Applications of Quantum Computers . . . . .	11
2.5	Quantum Error Correction . . . . .	12
2.6	Physical Implementations . . . . .	13
2.6.1	Ion traps . . . . .	14
2.6.2	Bulk Nuclear Magnetic Resonance . . . . .	14
2.6.3	Quantum Dots . . . . .	14
2.6.4	Cavity Quantum Electrodynamics (Cavity QED) . . . . .	15
2.6.5	Rare-Earth-Ion Doped Crystals . . . . .	15
2.6.6	Other Proposals . . . . .	15
<b>3</b>	<b>The Bloch Vector Formalism and Coherent Transient Phenomena</b>	<b>17</b>
3.1	Bloch Vector Representation of a Two-Level Quantum System . . . . .	17
3.2	Lifetime and Decoherence . . . . .	21
3.3	$\pi$ Pulses and $\pi/2$ Pulses . . . . .	22
3.4	Coherent Transient Phenomena . . . . .	22
3.4.1	Introduction . . . . .	22
3.4.2	Free Induction Decay . . . . .	22
3.4.3	The Two-Pulse Photon Echo . . . . .	23
3.4.4	The Three-Pulse Photon Echo . . . . .	23
<b>4</b>	<b>The Rare Earth Ion Quantum Computer</b>	<b>27</b>
4.1	Introduction . . . . .	27
4.2	Properties of $\text{Pr}^{3+}:\text{Y}_2\text{SiO}_5$ . . . . .	27
4.2.1	Level structure . . . . .	28
4.3	Dephasing Mechanisms in $\text{Pr}^{3+}:\text{Y}_2\text{SiO}_5$ . . . . .	29
4.4	Representation of Qubits in the REQC . . . . .	30
4.5	Gate Operations in the REQC . . . . .	32
4.6	Readout . . . . .	35

---

<b>5</b>	<b>Equipment</b>	<b>37</b>
5.1	The Laser . . . . .	37
5.2	Modulators and Modulator Drivers . . . . .	38
5.2.1	Acousto-Optic Modulators . . . . .	38
5.2.2	Electro-Optic Modulators . . . . .	39
5.3	The Cryostat . . . . .	39
5.4	Detectors . . . . .	40
<b>6</b>	<b>Experiment and Results</b>	<b>43</b>
6.1	Experimental setup . . . . .	43
6.2	Experiments . . . . .	44
6.3	Data Evaluation . . . . .	46
6.4	Results . . . . .	48
6.5	Discussion . . . . .	50
<b>7</b>	<b>Conclusions and Outlook</b>	<b>53</b>
<b>8</b>	<b>Acknowledgements</b>	<b>55</b>
	<b>Bibliography</b>	<b>55</b>
<b>A</b>	<b>Pulse Sequences</b>	<b>61</b>
<b>B</b>	<b>Spectromag Operation</b>	<b>65</b>
B.1	Overview . . . . .	65
B.1.1	Hose Connections . . . . .	65
B.1.2	Electronics . . . . .	68
B.1.3	Allen Bradley Resistors . . . . .	68
B.2	Cooling the system . . . . .	69
B.3	Operating the system . . . . .	74
B.3.1	Operating the magnets . . . . .	74
B.3.2	Operating the VTI . . . . .	75
B.3.3	Operating the LPF . . . . .	76
B.4	Refilling the system . . . . .	76
B.5	Encountered Problems . . . . .	77
B.5.1	Wrong mouthpiece . . . . .	77
B.5.2	Faulty Transfer Tube . . . . .	77
B.5.3	Long Extension Pieces . . . . .	77
B.5.4	Bent Brass Tube . . . . .	77
B.5.5	Nitrogen Level Probe Malfunction . . . . .	78

# Chapter 1

## Introduction

### 1.1 Background

Quantum computers offer radically new ways to process information by utilizing quantum mechanical phenomena. In contrast to classical computers, in which information is represented as *bits*, which can have a value of either 0 or 1, a quantum computer uses *quantum bits*, or *qubits*, which, being quantum mechanical systems, can be in an arbitrary superposition of 0 and 1. This enables it to reach beyond the limits predicted by classical information theory, and it has been shown that quantum algorithms can solve certain problems more efficiently than any known classical algorithm.

But while there has been tremendous progress during the last decade concerning the theoretical foundation for quantum computing, it has proved to be extremely difficult to actually implement these ideas in a real physical device, and quantum computers that would be able to do practically useful calculations are still far from being realized. Currently, a number of concepts are being studied, e. g. ion traps, nuclear magnetic resonance of molecules in a liquid and high-Q optical cavities. The Photon Echo Group at the Division of Atomic Physics, Lund University, is currently working on a scheme where the qubits are represented by the states of rare earth ions doped into an inorganic crystal. Data processing is performed by manipulating the ions using laser light. Presently, a main candidate is praseodymium doped yttrium silicate ( $\text{Pr}^{3+}:\text{Y}_2\text{SiO}_5$ ). In this scheme, the hyperfine levels of the ground state are used to represent qubit states, and logical operations are carried out via transitions between the ground state hyperfine levels and the first optically excited state.

This concept is, like other quantum computer concepts, extremely sensitive to perturbations, and there are several processes that cause *decoherence*, meaning that the wave functions of the qubits undergo random phase jumps, which makes it impossible to do useful computations. There are error correcting schemes that can compensate for this, provided that the probability of error per gate operation is sufficiently small. An often used criterion is that there must be on average no more than one error per 10,000 gate operations. There are two coherence times

of interest here: The coherence time of the optical transition, which limits the accuracy of each gate operation, and the coherence time between the hyperfine levels, which limits the number of gate operations that can be made before correcting schemes have to be applied.

## 1.2 Goal

A major source of decoherence is spin-spin interaction between the Pr ions and atoms in the host material. One possibility to decrease their contribution to the decoherence is to apply an external magnetic field. The aim of this work was initially to investigate how the coherence times of both the optical and the hyperfine transitions are affected by magnetic fields of various strength, in an attempt to get closer to the ultimate goal of achieving coherence times of the order of 10,000 times longer than the time for one gate operation. Due to time constraints and experimental difficulties, only the optical coherence time has been measured.

## 1.3 Outline

The thesis starts in chapter 2 with an overview of quantum computing in general, including quantum registers, gates, algorithms and error correction, as well as physical realizations of these concepts. Chapter 3 describes the theory of 2-level quantum systems and photon echoes, which is necessary to understand both the experimental techniques used in this work and the techniques used in the rare earth computer concept in general. A detailed description of the rare earth quantum computer is given in chapter 4.

In chapter 5, a description of the equipment used is given, followed by the experimental procedure in chapter 6. This chapter also contains results and a discussion. Finally, in chapter 7, some suggestions for further investigations are given.

The report also contains an appendix that gives a more detailed description of the pulse sequences used, and an appendix that gives detailed information about how to operate the groups's Oxford Instruments Spectromag cryostat. Putting the Spectromag into operation was one of the author's main responsibilities. The aim of this appendix is to help future operators to avoid mistakes that could consume a lot of valuable time.

## Chapter 2

# Quantum Computing

### 2.1 History of Quantum Computing

The idea that quantum systems can be used for information processing in a radically different way than is possible with classical systems is rather new, and can possibly be traced back to the 1980s, when R. Feynman pointed out that classical computers seem to be unable to simulate a quantum system efficiently. A quantum system, on the other hand, would be able to efficiently simulate another quantum system.[1] By *efficiently*, it is meant that the algorithm has at most a polynomial time complexity, which means that the number of computational steps required has a polynomial dependence on the input size. An algorithm that has an exponential time complexity is considered inefficient. This led D. Deutsch to ask whether a quantum system would be able to make computations more efficiently than a classical computer, and in 1985 he presented what is considered to be the first description of a quantum computer [2]. However, only very few problems could be shown to be solved more efficiently on a quantum computer, and these problems were rather contrived. A major breakthrough occurred in 1994 when P. Shor presented his now famous algorithm for factoring numbers and computing discrete logarithms [3]. This sparked great interest in the field, and much research has since then been done to make experimental realizations of quantum computing.

### 2.2 Qubits and Quantum Registers

The smallest unit of information in classical computing is the *bit*, which can be either in state 0 or state 1. The equivalent unit in quantum computing is the *quantum bit* or *qubit*. As the qubit is a quantum mechanical system, it can be not only in state  $|0\rangle$  or  $|1\rangle$ <sup>1</sup>, but also in an arbitrary superposition of the two states. Thus, the general state of a qubit can be written as:

$$\Psi = \alpha|0\rangle + \beta|1\rangle \tag{2.1}$$

---

<sup>1</sup>In quantum computing, states are usually written using the Dirac bra-ket notation.

where the coefficients  $\alpha$  and  $\beta$  are complex numbers.  $|\alpha|^2$  and  $|\beta|^2$  are the probabilities of finding the system in state  $|0\rangle$  and  $|1\rangle$  respectively. Consequently,  $|\alpha|^2 + |\beta|^2 = 1$ . The argument of a coefficient represents the phase of the corresponding state. A number of qubits together makes up a *quantum register*. The state of a quantum register is written using the format  $|ijk\dots\rangle$ , where  $i$  is the state of the  $i$ :th qubit. As an example, the state of a 2-qubit register can be written as:

$$\Psi = \alpha|00\rangle + \beta|01\rangle + \gamma|10\rangle + \delta|11\rangle \quad (2.2)$$

Generally, an  $n$ -qubit register can be in a superposition of  $2^n$  states. Thus, by using such a superposition as input to an algorithm,  $2^n$  different inputs can be processed at the same time. This phenomenon is known as *quantum parallelism*, and in this it can be intuitively understood why quantum computers are more powerful than classical computers. However, when reading out the results of a calculation, the quantum computer will only provide an answer for one input state, which is chosen at random. This is because of the measurement postulate of quantum mechanics; by reading out the result of a calculation, we perform a measurement on the register, and this causes the state to collapse.[4] Because of this, it is not immediately clear that quantum computers can be used for practical computations. However, a number of useful quantum algorithms have been invented, and some of these will be presented in the following sections.

## 2.3 Quantum Gates

A classical computer uses logical gates such as the AND, OR and NOT gates to perform computations. In quantum computing, *quantum gates* are used. The classical set of gates is not directly applicable for quantum computing because these gates are irreversible. This means that once a gate has been applied, it is generally not possible to tell what was the input state. For example, a classical AND operation is irreversible, because if the output is a 0, there is no way to know whether the input was 00, 01 or 10<sup>2</sup>. A quantum gate is a time evolution of a closed quantum system, which is always reversible as it is governed by the Schrödinger equation. An irreversible gate would necessarily mean that the system is not closed, i.e. there is unwanted interaction between the qubits and their environment.

Much research has been done concerning how many and how complex gate operations are required to form a *universal set*. A universal set is a set of gates which, when combined, can perform an arbitrary logical operation. The results are encouraging: It has been shown that a number of single-qubit operations and one two-qubit operation is enough.[5] This makes it easier to implement the computer: Only one two-qubit gate has to be made to work, and while a number of single-qubit gates are required, they are generally much easier to implement. One single-qubit gate is the *phase gate*  $P(\theta)$  which transforms the state  $\alpha|0\rangle + \beta|1\rangle$  to  $\alpha|0\rangle + e^{i\theta}\beta|1\rangle$ , or in matrix form:

$$P(\theta) = \begin{bmatrix} 1 & 0 \\ 0 & e^{i\theta} \end{bmatrix} \quad (2.3)$$

<sup>2</sup>Note that it is possible to construct classical reversible logic too, but it is not used in ordinary computers.

Another important single-qubit gate is the *Hadamard gate*  $H$ , which changes a qubit in the  $|0\rangle$  state to an equal superposition of  $|0\rangle$  and  $|1\rangle$ , or more generally:

$$H = \frac{1}{\sqrt{2}} \begin{bmatrix} 1 & 1 \\ 1 & -1 \end{bmatrix} \quad (2.4)$$

One example of a two-qubit gate that would form a universal set together with the single-qubit gates discussed above is the *Controlled-Not*, or *CNOT*, which takes one *control qubit* and one *target qubit* as input, and inverts the target qubit if and only if the control qubit is 1. In general, this means that the following transformation occurs:

$$\alpha|00\rangle + \beta|01\rangle + \gamma|10\rangle + \delta|11\rangle \longrightarrow \alpha|00\rangle + \beta|01\rangle + \delta|10\rangle + \gamma|11\rangle \quad (2.5)$$

Or in matrix formulation:

$$CNOT = \begin{bmatrix} 1 & 0 & 0 & 0 \\ 0 & 1 & 0 & 0 \\ 0 & 0 & 0 & 1 \\ 0 & 0 & 1 & 0 \end{bmatrix} \quad (2.6)$$

Note that there are other two-qubit gates that could be used to form a universal set. However, the CNOT is the gate that is most commonly encountered in literature.

## 2.4 Applications of Quantum Computers

The most famous quantum algorithm is *Shor's algorithm* for finding the prime factors of integers and computing discrete logarithms. Its importance lies in the fact that many modern cryptographic schemes rely on the fact that there are no known efficient classical algorithms for number factorization and discrete logarithm computations. Examples of these are the well known RSA (Rivest-Shamir-Adleman) system for encryption and digital signatures (number factorization) and the Diffie-Hellman key exchange protocol (discrete logarithms) [6]. While the best known classical factoring algorithm, the *number field sieve*, has a time complexity between polynomial and exponential time, Shor's algorithm has a polynomial time complexity, which makes factorization roughly as efficient as multiplication, making the RSA system completely insecure. However, it should be noted that it has never been proved there does not exist efficient classical factoring algorithms.[3]

Another useful algorithm is *Grover's algorithm* for database search. The problem it addresses can generally be stated: Given a function  $y = f(x)$  and an output  $y$ , what was the input  $x$ ? This is equivalent to searching an unsorted database (where  $y$  is the search criterion and  $x$  is the address of the entry to be found), and while the best classical algorithm is a linear search, with a linear time complexity, Grover's algorithm can accomplish the task in  $O(\sqrt{n})$  steps. In this case the speedup is provable, although it is less dramatic than in Shor's algorithm.[7] Grover's algorithm is also useful in cryptology, as it can be used to defeat a cipher by an *exhaustive key search*, where all possible keys are tested in order to find the right one, in  $O(\sqrt{n})$  time.

Another important application is to simulate quantum mechanical systems. As more and more nano-scale technology is being developed, quantum mechanical effects are beginning to be noticeable in engineered systems. The ability to accurately predict the properties of quantum systems will become even more important in the future, and as mentioned earlier, it is not possible to do efficient simulations of quantum systems today, using classical computers. Because of this, precise simulations can be done only for very small systems. Otherwise, major approximations need to be done. With quantum computers, this problem might be greatly alleviated.

## 2.5 Quantum Error Correction

In classical information theory, error correcting codes are an important field of study that enables reliable transmission of information even over non-perfect communication channels. The simplest way to do that is to transmit each bit a number of times. The receiver then counts the number of received ones and zeros, and assumes that the majority of received bits is right. More generally, the data can be divided into sequences of  $k$  bits. Each such bit is then substituted by a sequence of  $n$  bits, where  $n > k$ . The  $n$ -bit sequences are chosen such that they differ from each other in as many places as possible. If a few bits are corrupted on their way to the receiver, the received  $n$ -bit sequence should not be valid, and the receiver can request that the data is retransmitted. Needless to say, these schemes work only if the probability of error is sufficiently low; if too many bits are corrupted, the transmitted sequence might be valid, although not the intended one.

Experimental realizations of quantum computers are not very accurate and suffer from limited coherence times. No matter how much technology advances, the coherence times in a physical system will always be finite. Therefore, it is crucial to perform error correction of the internal state of the computer during a computation. For a long time, it was not known if it was possible at all to construct quantum equivalents to classical correction codes. The problem lies in the fact that we are not allowed to measure the state of the computer before the computation is finished; doing so would destroy the superposition. In addition, correcting an arbitrary superposition of states is much more challenging than correcting a classical bit that have only two possible states. The naive implementation, to use a number of physical qubits to represent each logical qubit and then perform error correction by majority vote on these would therefore not work. However, from the middle of the 90's and onwards, a number of feasible quantum error correction codes have been invented. In short, error correction can be performed by a modification of the classical scheme described above, where a  $k$ -bit word is represented by a longer  $n$ -bit word. In the quantum case, a further number of bits, known as ancilla bits, are introduced to store error information. To perform an error correction operation, an *error syndrome extraction* operation is performed such that the ancilla bits contain information about the error *without* containing information about the actual state of the quantum register. It is then possible to correct the error without directly measuring the state of the register. As in the classical case, a certain quantum

error correction scheme works only if the probability of error in the underlying hardware is sufficiently small.[8]

## 2.6 Physical Implementations

A wide variety of physical systems have been proposed as candidates for quantum computers. Here, some of the most important ones will be briefly described. D. DiVincenzo has formulated five requirements for physical implementations of quantum computers [9]:

1. The computer must be scalable and have well-characterized qubits. The scalability requirement means that it must be possible to scale up the computer to an arbitrarily large number of qubits and computational steps. This is a tough requirement, because the two-qubit gates must be able to operate on any two qubits, which means that each added qubit must be able to interact with all the others. *Well-characterized* means, among other things, that its Hamiltonian is accurately known, as well as the coupling to other qubits and any externally applied fields. If the system used as a qubit has more than two states, one must choose which two to use as  $|0\rangle$  and  $|1\rangle$ , and one must make sure that the probability of the system going into another state is small.
2. It must be possible to initialize the quantum register to a well-defined state, such as  $|000\dots\rangle$ . This is rather obvious: To do useful calculations, the computer must be in a known state at the start of a computation. Quantum error correction schemes also need a continuous supply of initialized qubits.
3. The coherence time of the qubits must be much longer than the gate operation time. Decoherence is caused by unwanted interaction between the qubits and the environment, and is manifested by random phase jumps of the qubits. This destroys the quantum properties of the system, making the computation useless. It is often stated that a coherence time of  $10^4$ – $10^5$  times the gate operation time is required. Once this is achieved, quantum error correction schemes can efficiently eliminate any remaining errors. This has proved to be a major obstacle in the attempts to realize quantum computers, because quantum systems are seldom even close to meeting this requirement.
4. There must be a universal set of gates. As stated earlier, this requires a number of single-qubit gates that can act on any qubit as well as one two-qubit gate that can operate on any two qubits. The gate operations must be designed to eliminate any systematic errors as much as possible. When it comes to random errors, they should have a probability of no more than  $10^{-4}$ – $10^{-5}$  per operation.
5. It must be possible to read out the qubits at the end of the computation. Ideally, a measurement on a qubit in state  $\alpha|0\rangle + \beta|1\rangle$  should yield 0 with probability  $|\alpha|^2$  and 1 with probability  $|\beta|^2$ , and should not affect the state of the other qubits, except for changes caused by entanglement.

Now follows a list of candidates for quantum computing. It is by no means exhaustive, and is merely meant to illustrate the great variety of proposals for physical implementations of qubits and gates.

### 2.6.1 Ion traps

In this scheme, a number of ions is placed in a linear ion trap such as a *Paul trap*, where they are kept in place by a radio-frequency (RF) field.[4] The ions are cooled to their lowest vibrational state using laser light. Each ion represents a qubit, where two suitably selected atomic levels represent  $|0\rangle$  and  $|1\rangle$ . Qubits can be initialized by optically pumping them to the desired state. One-qubit gates are implemented by driving the transition between the levels using laser light. For two-qubit gates such as the CNOT, the vibrational modes of the ions in the trap are used. When one qubit changes its internal state, it will also change the vibrational mode of the chain of ions, which couples to the other ions.[10]

### 2.6.2 Bulk Nuclear Magnetic Resonance

Here, a complex molecule that includes a number of atoms with nuclear spin  $1/2$  is used. Each such nucleus represents a qubit, with the two spin states representing  $|0\rangle$  and  $|1\rangle$ . The molecule is subjected to a strong magnetic field, which causes a Zeeman splitting of the two spin states, typically in the RF region. The nuclei will have slightly different resonance energies, as they have different chemical environments, and this means that it is possible to address individual qubits using RF pulses which match their frequency. Two-qubit gates are implemented utilizing the fact that the resonance frequency of a nucleus depends on the state of its neighbors. In principle, a single molecule can be used as a computer, but the readout signal would then be extremely weak. In practice, billions of molecules are operated on simultaneously.[11]

This type of quantum computer performed the very first demonstration of Shor's algorithm in 2001, when a group of IBM scientists and graduate students from Stanford University factored the number 15, using a custom-made molecule consisting of five  $^{19}\text{F}$  and two  $^{13}\text{C}$  atoms.[12]

### 2.6.3 Quantum Dots

A quantum dot is an artificially created potential well, typically implemented in a semiconductor crystal, that can hold one or many electrons. The well dimensions are of the same order of magnitude as the de Broglie wavelength of the electrons. The quantum dot thus has an energy structure not unlike that of an atom.

It has been proposed that a quantum computer could be implemented by using single-electron quantum dots as qubits, where the spin state of the electron represents the qubit state. It is possible to control the potential barrier between adjacent quantum dots by electrical means. Thus, by lowering the barrier between selected quantum dots, qubits can be made to interact, which makes it possible to implement two-qubit gates. One-qubit gates could be implemented by applying an external magnetic field to the selected qubit with the help of a scanning-probe tip. Another possibility is to have a magnetized region in the vicinity of the quantum dots, with a controllable potential barrier between the

dots and this region. By lowering this barrier, the selected electron could be made to interact with the magnetized region for a suitably selected amount of time.[13]

#### 2.6.4 Cavity Quantum Electrodynamics (Cavity QED)

Here, the qubit is represented as the state of the electrical field in an optical cavity, where  $|0\rangle$  means that no photon is present, and  $|1\rangle$  means that one photon is present. A quantum register is built by using a large number of such cavities, and two-qubit gates are realized by sending atoms through the cavities. For a CNOT gate, the atom first interacts with the electric field of the cavity used as the control qubit, which changes the atomic state. The atom then proceeds to the target qubit, where it interacts with the electric field of that cavity. Atoms are also used to realize one-qubit gates. In this case, they only pass through one cavity.[14]

#### 2.6.5 Rare-Earth-Ion Doped Crystals

This is the concept that is being studied by the Photon Echo Group at Lund University. It is described in detail in chapter 4.

#### 2.6.6 Other Proposals

Many other concepts are being studied, including superconducting quantum interference devices (SQUIDs) [15], electrons on liquid helium [16], molecular magnets [17] and fullerene-based electron spin resonance [18].



## Chapter 3

# The Bloch Vector Formalism and Coherent Transient Phenomena

### 3.1 Bloch Vector Representation of a Two-Level Quantum System

*“To understand something means to derive it from quantum mechanics, which nobody understands.”*

– Proverbial among physicists

The Bloch vector formalism is an elegant and powerful way to describe a two-level quantum system. It will be treated in some detail here, because it is a very convenient way to describe the photon echo process, which has been used extensively in the laboratory work. Here, it is used to describe two optical levels of an atom, which is interacting with laser radiation. However, it is a very general description and can be used for any two-level quantum system. The description presented here largely follows that of Foot [4], with a slightly changed sign convention:

Consider a two-level atom described by the Hamiltonian  $H_0$ . The stationary state  $\Psi_n$  with energy  $E_n$  can be written as:

$$\Psi_n(\mathbf{r}, t) = \psi_n(\mathbf{r})e^{-iE_n t/\hbar} \quad (3.1)$$

The atom can be in a superposition of these states, so in general its wave function can be written as:

$$\Psi(\mathbf{r}, t) = c_1(t)\psi_1(\mathbf{r})e^{-iE_1 t/\hbar} + c_2(t)\psi_2(\mathbf{r})e^{-iE_2 t/\hbar} \quad (3.2)$$

where  $c_1(t)$  and  $c_2(t)$  are time-dependent coefficients satisfying  $|c_1(t)|^2 + |c_2(t)|^2 = 1$ . Suppose the atom interacts with an oscillating electric field (for example a

## 18 The Bloch Vector Formalism and Coherent Transient Phenomena

laser beam) with amplitude  $E_0$  and frequency  $\omega$ . This can be described by the Hamiltonian

$$H_I(t) = e\mathbf{r} \cdot \mathbf{E}_0 \cos(\omega t) \quad (3.3)$$

where  $e$  is the elementary charge.

Using the time-dependent Schrödinger equation

$$i\hbar \frac{\partial \Psi}{\partial t} = H\Psi = (H_0 + H_I(t))\Psi \quad (3.4)$$

and inserting 3.2 into 3.4, we get

$$\begin{aligned} i \frac{dc_1}{dt} &= \Omega \cos(\omega t) e^{-i\omega_0 t} c_2 \\ i \frac{dc_2}{dt} &= \Omega^* \cos(\omega t) e^{i\omega_0 t} c_1 \end{aligned} \quad (3.5)$$

where  $\omega_0 = (E_2 - E_1)/\hbar$  and the *Rabi frequency*  $\Omega$  is

$$\Omega = \frac{\langle 1 | e\mathbf{r} \cdot \mathbf{E}_0 | 2 \rangle}{\hbar} \quad (3.6)$$

These equations can be rewritten as:

$$\begin{aligned} i \frac{dc_1}{dt} &= c_2 \left\{ e^{i(\omega - \omega_0)t} + e^{-i(\omega + \omega_0)t} \right\} \frac{\Omega}{2} \\ i \frac{dc_2}{dt} &= c_1 \left\{ e^{-i(\omega - \omega_0)t} + e^{i(\omega + \omega_0)t} \right\} \frac{\Omega^*}{2} \end{aligned} \quad (3.7)$$

Now, we assume that the terms with exponents  $\omega + \omega_0$  oscillate fast enough so that they average to zero on the time scales of interest, and thus, these terms can be neglected. This is known as the *rotating-wave approximation*. We also introduce the *detuning*  $\delta$ , defined as  $\delta = \omega - \omega_0$  — the difference between the laser frequency and the frequency of the atomic transition. Now, we can write the equations above as:

$$\begin{aligned} i \frac{dc_1}{dt} &= c_2 e^{i\delta t} \frac{\Omega}{2} \\ i \frac{dc_2}{dt} &= c_1 e^{-i\delta t} \frac{\Omega^*}{2} \end{aligned} \quad (3.8)$$

The electric field induces an electric dipole moment  $\mathbf{D}$  in the atom. Assuming that the electric field is in the  $\mathbf{e}_x$  direction, the expectation value of the electric dipole moment is:

$$-eD_x(t) = - \int \Psi^\dagger(t) e x \Psi(t) d^3 \mathbf{r} \quad (3.9)$$

Inserting equation 3.2 into 3.9, the electric dipole moment becomes:

$$\begin{aligned} -eD_x(t) &= -e \int (c_1 e^{-i\omega_1 t} \phi_1 + c_2 e^{-i\omega_2 t} \phi_2)^* x (c_1 e^{-i\omega_1 t} \phi_1 + c_2 e^{-i\omega_2 t} \phi_2) d^3 \mathbf{r} = \\ &= -e \{ c_2^* c_1 X_{21} e^{i\omega_0 t} + c_1^* c_2 X_{12} e^{-i\omega_0 t} \} \end{aligned} \quad (3.10)$$

### 3.1 Bloch Vector Representation of a Two-Level Quantum System 19

where

$$X_{12} = \langle 1|x|2 \rangle \quad (3.11)$$

From this we can see that the electric dipole moment depends on the quantities  $c_1^*c_2$  and  $c_2^*c_1$ . Now, we introduce the *density matrix* for the state of the atom, defined as:

$$|\Psi\rangle\langle\Psi| = \begin{pmatrix} c_1 \\ c_2 \end{pmatrix} \begin{pmatrix} c_1^* & c_2^* \end{pmatrix} = \begin{pmatrix} |c_1|^2 & c_1c_2^* \\ c_2c_1^* & |c_2|^2 \end{pmatrix} = \begin{pmatrix} \rho_{11} & \rho_{12} \\ \rho_{21} & \rho_{22} \end{pmatrix} \quad (3.12)$$

Obviously, the diagonal elements are the populations. The off-diagonal elements are *coherences* and are related to the phase of the wave functions.

Now,  $c_1$  and  $c_2$  are substituted for:

$$\begin{aligned} \tilde{c}_1 &= c_1 e^{-i\delta t/2} \\ \tilde{c}_2 &= c_2 e^{i\delta t/2} \end{aligned} \quad (3.13)$$

We can also write  $\tilde{\rho}_{12} = \rho_{12} e^{-i\delta t}$  and  $\tilde{\rho}_{21} = \rho_{21} e^{i\delta t}$ . Assuming that  $X_{12}$  is real, which is true for transitions between two bound states of an atom, equation 3.10 can be written as

$$-eD_x(t) = -eX_{12} \{ \tilde{\rho}_{12} e^{i\omega t} + \tilde{\rho}_{21} e^{-i\omega t} \} = -eX_{12} (u \cos \omega t + v \sin \omega t) \quad (3.14)$$

Here,  $\tilde{\rho}_{12}$  and  $\tilde{\rho}_{21}$  have been substituted by the new variables  $u$  and  $v$  according to:

$$\begin{aligned} u &= \tilde{\rho}_{12} + \tilde{\rho}_{21} \\ v &= i(\tilde{\rho}_{12} - \tilde{\rho}_{21}) \end{aligned} \quad (3.15)$$

The physical interpretation of this is that  $u$  is the part of the electric dipole moment that is oscillating in phase with the incoming laser light, while  $v$  is the quadrature part of the electric dipole moment — oscillating  $90^\circ$  out of phase with the laser.

In order to find expressions for  $u$  and  $v$ , we turn back to equations 3.8. Inserting the variables introduced in equation 3.13, they can be rewritten as:

$$\begin{aligned} i \frac{d\tilde{c}_1}{dt} &= \frac{1}{2}(\delta\tilde{c}_1 + \Omega\tilde{c}_2) \\ i \frac{d\tilde{c}_2}{dt} &= \frac{1}{2}(\Omega\tilde{c}_1 - \delta\tilde{c}_2) \end{aligned} \quad (3.16)$$

This can also be expressed using the variables  $\rho_{11}$ ,  $\rho_{22}$ ,  $\tilde{\rho}_{12}$  and  $\tilde{\rho}_{21}$  according to:

$$\begin{aligned} \frac{d\tilde{\rho}_{12}}{dt} &= \left( \frac{d\tilde{\rho}_{21}}{dt} \right)^* = -i\delta\tilde{\rho}_{12} + \frac{i\Omega}{2}(\rho_{11} - \rho_{22}) \\ \frac{d\rho_{22}}{dt} &= -\frac{d\rho_{11}}{dt} = \frac{i\Omega}{2}(\tilde{\rho}_{21} - \tilde{\rho}_{12}) \end{aligned} \quad (3.17)$$

Now, we introduce a new variable  $w$ , defined as the level of inversion,  $w = \rho_{22} - \rho_{11}$ . Expressing equations 3.17 in terms of  $u$ ,  $v$  and  $w$ , we finally arrive at

## 20 The Bloch Vector Formalism and Coherent Transient Phenomena

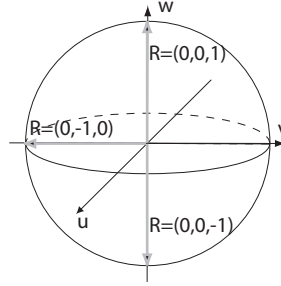


Figure 3.1: A Bloch sphere, with three different states shown.  $R = (0,0,-1)$  is the ground state,  $R = (0,0,1)$  is the excited state and  $R = (0,-1,0)$  is a coherent superposition of states, with a phase difference of  $-90^\circ$  in relation to the reference phase.

the optical Bloch equations:

$$\begin{aligned}\frac{du}{dt} &= -\delta v \\ \frac{dv}{dt} &= \delta u + \Omega w \\ \frac{dw}{dt} &= -\Omega v\end{aligned}\tag{3.18}$$

Note that this model does not account for the finite lifetime of the higher-lying state or limited coherence times. They can be included by inserting additional terms into the equations. The state of the system is completely described by  $u$ ,  $v$  and  $w$ , and they are often combined to the *Bloch vector*:

$$\mathbf{R} = (u, v, w)\tag{3.19}$$

We also define a vector, sometimes referred to as the *pseudo-vector* [19] as:

$$\mathbf{W} = (-\Omega, 0, \delta)\tag{3.20}$$

The pseudo-vector describes how the system is driven by an externally applied field, such as light from a laser, with the Rabi frequency  $\Omega$  and the detuning  $\delta$ . Now, the optical Bloch equations can be written in a very compact form:

$$\frac{d\mathbf{R}}{dt} = \mathbf{W} \times \mathbf{R}\tag{3.21}$$

Note that the quantity  $\mathbf{W} \times \mathbf{R}$  always is perpendicular to both  $\mathbf{R}$  and  $\mathbf{W}$ . This means that  $\frac{d\mathbf{R}}{dt} \cdot \mathbf{R} = 0$ , so the length of  $\mathbf{R}$  is constant — it can be shown that it is equal to 1. This means that the Bloch vector will always correspond to points on a sphere with unit radius, the *Bloch sphere*. The Bloch sphere is a very common way to visualize the state of a two-level quantum system. An example of a Bloch sphere can be seen in figure 3.1. Now we need a physical interpretation of the components of the Bloch sphere. The role of  $w$  is quite straightforward — it represents the level of inversion.  $w = -1$  corresponds to the atom being in the ground state,  $w = 1$  means that it is in the excited state,

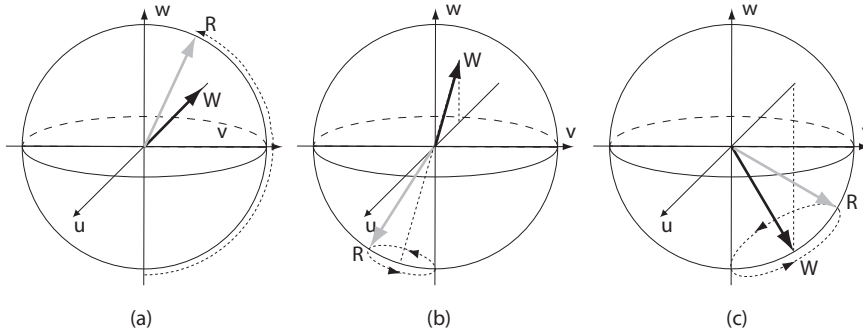


Figure 3.2: A 2-level system initially in the ground state that is being driven (a) at resonance. The system will be driven between the ground state and the excited state. (b) with positive detuning. (c) with negative detuning. In the last two cases, complete population inversion can not be achieved.

and  $w = 0$  means that it is in an equal superposition of the ground state and excited state.

The  $u$  and  $v$  components represent the phase of the atomic state. As was described earlier, an atom in a coherent superposition has an oscillating electric dipole moment, and it is the phase of this dipole moment that is described by  $u$  and  $v$ ,  $u$  being the component that is in phase with the driving laser field and  $v$  being the component that is  $90^\circ$  out of phase with this field.

When laser light is applied, the Bloch vector will rotate in a plane perpendicular to  $\mathbf{W}$  with an angular frequency that is proportional to the magnitude of  $\mathbf{W}$ . For a laser pulse with duration  $t$ , the Bloch vector will move an angle:

$$\theta = \sqrt{\Omega^2 + \delta^2} \cdot t \quad (3.22)$$

The quantity  $\sqrt{\Omega^2 + \delta^2}$  is known as the *generalized Rabi frequency*, and  $\theta$  is called the *pulse area*. The effect of applying laser fields with different detunings can be found in figure 3.2.

## 3.2 Lifetime and Decoherence

In the discussion in the previous section, two important factors have been neglected: In reality, the upper state has a finite lifetime, designated  $T_1$ , and furthermore, the transition has a finite *coherence time*, designated  $T_2$ .  $1/T_1$  is the rate with which the atoms relax through spontaneous emission and is determined by the oscillator strength of the transition.  $1/T_2$  is the rate at which the atoms make random phase jumps and lose coherence due to interactions with their environment. The mechanisms involved in the coherence loss are different for different systems. The most important decoherence mechanisms in the  $\text{Pr}^{3+}:\text{Y}_2\text{SiO}_5$  crystal are discussed in chapter 4. The effects of the limited life-

## 22 The Bloch Vector Formalism and Coherent Transient Phenomena

time and coherence time can be included in the Bloch equations as follows: [19]

$$\begin{aligned}\frac{du}{dt} &= -\delta v - \frac{u}{T_2} \\ \frac{dv}{dt} &= \delta u + \Omega w - \frac{v}{T_2} \\ \frac{dw}{dt} &= -\Omega v - \frac{w - w_{\text{eq}}}{T_1}\end{aligned}\tag{3.23}$$

where  $w_{\text{eq}}$  is the equilibrium value of  $w$ , often close to  $-1$ .

### 3.3 $\pi$ Pulses and $\pi/2$ Pulses

Consider an atom initially in the ground state,  $\mathbf{R} = (0, 0, -1)$ . If a pulse with pulse area  $\theta = \pi$ , is applied exactly on resonance with the atom, the atom will be driven to the excited state  $\mathbf{R} = (0, 0, 1)$ . This kind of pulse is known as a  $\pi$  pulse. A pulse with pulse area  $\pi/2$ , known as a  $\pi/2$  pulse, will drive an atom initially in the ground state to an equal superposition of the ground state and the excited state.  $\pi$  pulses and  $\pi/2$  pulses play a significant role in photon echo processes, which will be described later in this chapter.

## 3.4 Coherent Transient Phenomena

### 3.4.1 Introduction

This section covers a number of phenomena that can be observed in quantum systems with long coherence times. Another necessary criterion is that the system under study has a large inhomogeneous broadening; that is, it consists of a large number of 2-level systems that each have a slightly different resonance frequency, which will cause the absorption profile of the whole ensemble to be considerably broader than the absorption profile of an individual 2-level system. The  $\text{Pr}^{3+}:\text{YSO}$  crystal is a good example of this, as the dopant Pr ions have coherence times on the order of  $100 \mu\text{s}$ , which means that the linewidth of individual ions is as small as a few kHz. The inhomogeneous absorption profile is on the other hand of the order of GHz [20].

### 3.4.2 Free Induction Decay

When an inhomogeneous ensemble of atoms is excited to a coherent superposition, it will emit radiation due to the oscillating electric dipole moment of the atoms. Just after the excitation pulse, all atoms will oscillate in phase with each other, producing coherent radiation. However, if the ensemble is inhomogeneously broadened, the atoms will oscillate at slightly different frequencies, and gradually dephase. This will cause the intensity of the emitted radiation to decrease exponentially, a phenomenon known as *free induction decay* (FID).

### 3.4.3 The Two-Pulse Photon Echo

The two-pulse photon echo is the basis of the experiment carried out during this work, so it is very important to have a clear understanding of the principles behind it. In this section, photon echoes will be described with the help of the Bloch sphere picture described earlier.

Assume that we have an inhomogeneously broadened ensemble of atoms initially in the ground state  $(0,0,-1)$ . If a  $\pi/2$  pulse is applied, the atoms will be excited to an equal superposition of the ground state and the excited state, where they are oscillating  $90^\circ$  out of phase with the laser field. Since the Bloch vector describes the phase in relation to the laser field, atoms exactly on resonance with the laser will stay in the same state as just after the application of the pulse. However, atoms not exactly on resonance will acquire a phase difference relative to the laser, and eventually the phases of the atoms will be spread out throughout the whole  $u-v$  plane.

After a time  $\tau_{12}$ , a  $\pi$  pulse is applied. After this, the Bloch vectors of the atoms are still in the  $u-v$  plane, but their relative phases will have been inverted, since the second pulse rotates them around the  $v$  axis. Since they continue to move in the  $u-v$  plane in the same way as before the pulse, the phase differences will now start to decrease, and after a time  $\tau_{12}$  after the second pulse, they will be in phase with each other again. Now, the radiation emitted by the individual atoms is in phase and interfere constructively. This causes a brief light pulse, a *photon echo*, to be emitted. The process is illustrated in figure 3.3. The two-pulse echo can be used to measure the coherence time  $T_2$  of the atoms. In such measurements, one utilizes the fact that in order to contribute to the echo, an atom must not lose coherence from the time the first pulse is applied to the time that the echo forms. The number of atoms that have not lost coherence during the time  $\tau$  is given by:

$$N = N_0 e^{-\tau/T_2} \quad (3.24)$$

The time between the first pulse and the echo is  $2\tau_{12}$ . Furthermore, the quantity that is usually measured is the light intensity, which is proportional to the square of the number of atoms in the case of coherent emission. The intensity of the echo  $I$  is then given by:

$$I = I_0 e^{-4\tau_{12}/T_2} \quad (3.25)$$

By measuring the intensity of the echo for various pulse separations, it is possible to fit the expression above to the measured data and obtain  $T_2$ .

### 3.4.4 The Three-Pulse Photon Echo

Three-pulse echoes have not been used in the experimental work of this thesis, but a discussion about photon echoes would be incomplete without a brief explanation of them. In a three-pulse echo, the atoms are first driven to the state  $(0,1,0)$  by a  $\pi/2$  pulse. Just as in the 2-pulse case, they gradually acquire a phase difference in relation to the laser, so that the Bloch vectors of the individual atoms are spread out in the  $u-v$  plane. After a time  $\tau_{12}$ , a second  $\pi/2$  pulse is applied. This will rotate the Bloch vector of the atoms either toward the upper or the lower state, depending on their phase at the time of the second

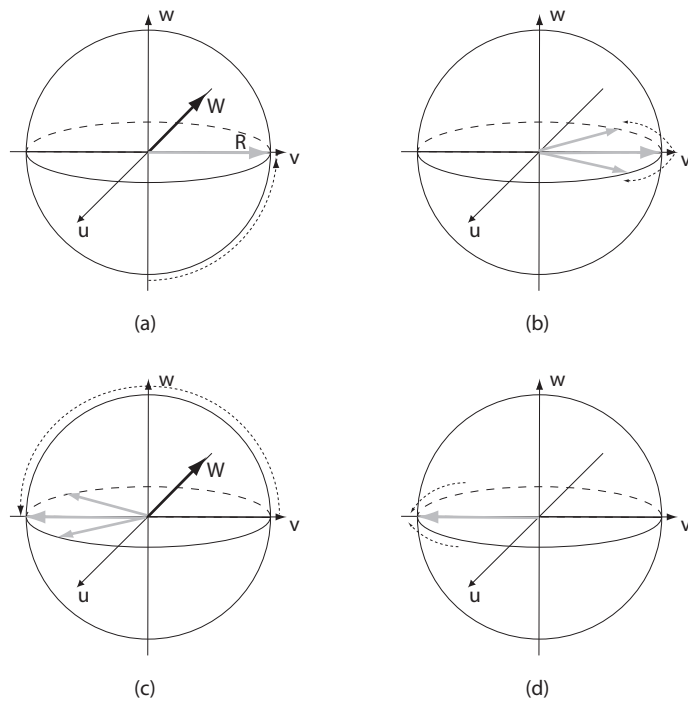


Figure 3.3: Bloch vector representation of a 2-pulse echo. (a) A  $\pi/2$  pulse rotates the Bloch vector to a superposition of states. (b) The atoms evolve freely during the time  $\tau_{12}$ . Since they have slightly different resonance frequencies, they will rotate around the Bloch sphere at different rates. (c) A  $\pi$  pulse changes the sign of the  $v$  component of all ions, inverting the phase differences between them. (d) After an additional time of  $\tau_{12}$ , the atoms will rephase, and they will briefly oscillate in phase, which causes a pulse of coherent light to be emitted.

pulse. Thus, the level of inversion of atoms with a particular frequency is given by this phase, and the two pulses create a periodic modulation of the population inversion in the frequency plane, known as a *population grating*.

After a time  $\tau_{23}$ , a third  $\pi/2$  pulse is applied. This will rotate the Bloch vectors back into the  $u$ - $v$  plane, and after a time  $\tau_{12}$  after the second pulse, they will rephase and create a *stimulated echo*.

3-pulse echoes can usually be performed on a longer timescale than 2-pulse echoes, since the time and phase information during the time  $\tau_{23}$  is encoded in the population density of the ground and excited state rather than the phase of the atoms. Therefore, the time that this information can be retained by the ions is determined not only by  $T_2$  but also by  $T_1$ , which is usually substantially longer.

## 26 The Bloch Vector Formalism and Coherent Transient Phenomena

## Chapter 4

# The Rare Earth Ion Quantum Computer

### 4.1 Introduction

The heart of the rare earth quantum computer (REQC) is an inorganic crystal, which has been doped with rare earth ions. The dopant ions are used as qubits, while the crystal itself serves merely as a host material for the ions.

The material that has been under study for this thesis is yttrium orthosilicate,  $\text{Y}_2\text{SiO}_5$ , often called YSO, which has been doped with Praseodymium ions with a concentration of approximately 0.005%.

### 4.2 Properties of $\text{Pr}^{3+}:\text{Y}_2\text{SiO}_5$

YSO is a crystal belonging to the  $C_{2h}^6$  space group. A unit cell of the crystal contains eight formula units and has the dimensions  $a = 10.410 \text{ \AA}$ ,  $b = 6.721 \text{ \AA}$  and  $c = 12.490 \text{ \AA}$  [20, 21]. The angle between  $a$  and  $c$  is  $102.39^\circ$ , while  $b$  is perpendicular to  $a$  and  $c$ . There are also two extinction axes at right angles to  $b$  and to each other, that are denoted D1 and D2. Light that is polarized along the extinction axes will keep its polarization. Light polarized in other directions will generally change its polarization due to birefringence. Figure 4.1 shows the geometry of these axes.[22] Some of the reasons for why it is one of the main candidates as a host crystal are that large crystals of good quality are readily available [20] and that the nuclear spin of the host crystal is small — yttrium has a nuclear spin of  $1/2$ , while the most abundant isotopes of silicon and oxygen have zero spin. This minimizes coherence loss due to nuclear spin interactions between the Pr ions and the host crystal [23].

Praseodymium is a rare earth metal with atomic number 59. The only naturally occurring isotope,  $^{141}\text{Pr}$ , has a nuclear spin of  $5/2$ . When praseodymium ions are doped into the YSO crystal, there are two inequivalent sites in the lattice

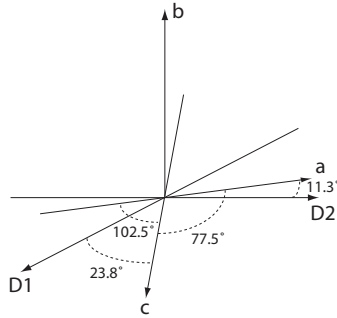


Figure 4.1: *Geometry of the axes in  $Pr^{3+}:Y_2SiO_5$ .*

that they can occupy, called site 1 and 2, which have a transition wavelength between the ground state and the first excited state of 605.98 nm and 607.93 nm respectively [20]. In the work presented here, only site 1 ions are considered. The reason for this is that the oscillator strength of the transition between the ground state and first excited state, which is used to perform quantum gate operations, is one order of magnitude lower for site 2 ions than for site 1 ions. This makes it much more difficult to drive the transition for site 2 ions.

#### 4.2.1 Level structure

When Pr is doped into a YSO crystal, it becomes a trivalent ion,  $Pr^{3+}$ , with configuration  $4f^26s^2$ . The ground state has the term symbol  $^3H_4$ , while the first excited state is denoted  $^1D_2$ . [24] Due to the crystal field, each term is split into a manifold of at most  $2J + 1$  Stark levels. In this case, only the lowest Stark level of each manifold is considered. The reason for this is that higher-lying levels usually relax quickly by phonon emission, making their lifetimes and coherence times unsuitable for quantum computing.

In addition to this, each Stark level is further split into hyperfine levels. There are two main mechanisms involved here: Electric quadrupole interaction and a second-order magnetic hyperfine interaction (also known as pseudo-quadrupole interaction) [19]. The electric quadrupole interaction arises due to the fact that the nucleus is not perfectly spherically symmetric. This gives the nucleus a *electric quadrupole moment*, since its charge is not symmetrically distributed. The energy of the atom will then depend on how this quadrupole moment is oriented in relation to the gradient of the electric field caused by the electrons. [25] The magnetic hyperfine interaction arises from interaction between the magnetic moment possessed by the electrons, caused by both spin and orbital angular momentum, and the magnetic moment of the nucleus.

The electronic angular momentum of the  $Pr^{3+}$  ion is quenched by the crystal field, and because of this,  $\mathbf{J} = 0$ . This means that the familiar first-order hyperfine shift, which is proportional to the product of the electronic angular momentum  $\mathbf{J}$  and the nuclear spin  $\mathbf{I}$ , does not exist here. However, by applying second-order perturbation theory, it can be shown that a hyperfine splitting indeed exists, and that the combined contribution to the Hamiltonian by this

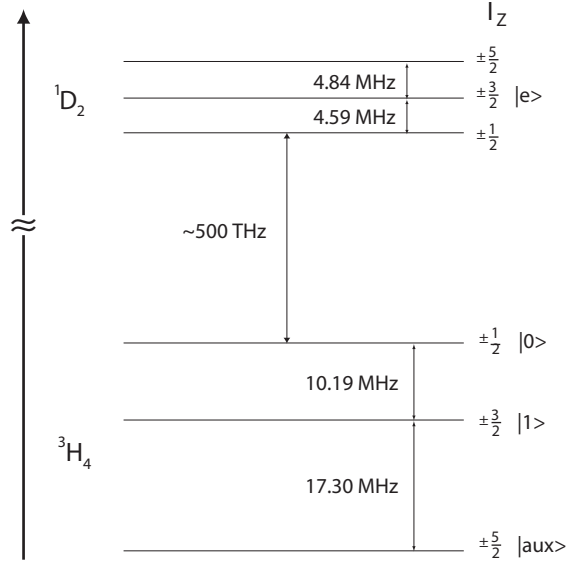


Figure 4.2: Level structure of  $\text{Pr}^{3+}:\text{Y}_2\text{SiO}_5$  at site 1 [26].

*second-order hyperfine shift* and the electric quadrupole interaction can be expressed as:

$$H_{hfs} = D_{hfs} \cdot (I_Z^2 - I(I+1)/3) + E_{hfs} \cdot (I_X^2 - I_Y^2) \quad (4.1)$$

where  $D_{hfs}$  and  $E_{hfs}$  are coupling constants and  $I_X$ ,  $I_Y$  and  $I_Z$  are projections of the nuclear spin along the selected quantization axes. For a more detailed treatment, see [27]. In both the ground state  ${}^3\text{H}_4$  and the excited state  ${}^1\text{D}_2$ , the energy structure consists of three doubly degenerate levels, labelled by the quantum number  $I_Z$  (see figure 4.2). In the presence of an external magnetic field, this degeneracy will be lifted.

### 4.3 Dephasing Mechanisms in $\text{Pr}^{3+}:\text{Y}_2\text{SiO}_5$

The homogeneous linewidth  $\Gamma_h$  of the optical transition is related to the coherence time according to:

$$\Gamma_h = \frac{1}{\pi T_2} \quad (4.2)$$

There are several dephasing mechanisms contributing to  $\Gamma_h$ . The ones that are commonly reported [20, 28] are:

- Population relaxation
- Emission, absorption and scattering of phonons
- Ion-ion interaction
- Ion-spin interaction

The linewidth can be written as a sum of these contributions:

$$\Gamma_h = \Gamma_{\text{pop}} + \Gamma_{\text{phonon}} + \Gamma_{\text{ion-ion}} + \Gamma_{\text{ion-spin}} \quad (4.3)$$

The contribution from relaxation is given by

$$\Gamma_{\text{pop}} = \frac{1}{2\pi T_1} \quad (4.4)$$

and is the ultimate limit of the coherence time. Dephasing due to phonons is the dominating dephasing mechanism for higher temperatures, but at the temperatures at which these experiments have been conducted (approximately 2 K), the contribution from phonons is significantly reduced [19].

Electric ion-ion interactions can play a significant role when a large number of dopant ions is excited, for example by an excitation pulse in a photon echo experiment. When an ion is excited, its electric dipole moment changes, which will perturb other ions in its vicinity, changing their resonance frequency. This is a process known as *instantaneous spectral diffusion*. An experimenter using photon echoes must be aware of the fact that the measurement itself introduces dephasing through this process.[20]

The fourth process,  $\Gamma_{\text{ion-spin}}$ , arises from interactions between the nuclear spin of the dopant ions and the host material. Nuclei with non-zero spin undergo spin flips, which causes the magnetic field in the crystal to fluctuate, which perturbs the dopant ions. This mechanism can partly be suppressed by applying an external magnetic field, which inhibits random spin flips.[19] It has earlier been reported that a small magnetic field (77 G) can decrease the linewidth by 500 Hz [20]. However, it is not well known how a strong magnetic field would affect the linewidth. It has also been reported that especially long coherence times between hyperfine levels can be achieved by applying a magnetic field at specific directions and magnitudes, known as “critical points”. When the magnetic field is applied, the hyperfine levels will split into Zeeman levels. At the critical points, the transition frequency between the hyperfine levels of interest is essentially independent of small magnetic field changes. This has been reported to give phase memory times of 82 ms [29].

## 4.4 Representation of Qubits in the REQC

The scheme to represent qubits relies on the fact that while the linewidth of the  ${}^3\text{H}_4 - {}^1\text{D}_2$  transition of a single ion is very narrow, on the order of kHz, the inhomogeneous spectral width of the whole ensemble in the crystal is on the order of GHz. The reason for this broadening is that due to imperfections in the crystal, the ions will experience slightly different crystal fields, and this will shift their transition frequencies by different amounts. The resonance frequency of a particular ion has in general no obvious dependence on its spatial position in the crystal. However, for ions lying very close to each other, the electric dipole-dipole interaction can be the primary inhomogeneous broadening mechanism. These ions have large frequency shifts and form so-called satellite lines that can be observed outside the main inhomogeneous absorption profile and in this case,

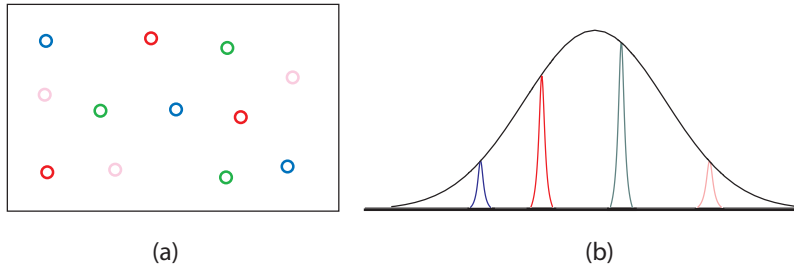


Figure 4.3: (a) Ions that have been randomly doped into the crystal and happen to have the same frequency ... (b) ... together make up a frequency channel inside the inhomogeneous absorption profile, and are used as a qubit.

there is a correlation between the resonance frequencies and the relative position of the ions. This phenomenon has been investigated in  $\text{Eu}^{3+}:\text{Y}_2\text{SiO}_5$  by Sellars et al [30], but has not been considered further in the description below.

The hyperfine levels  $I_Z = \pm 1/2$  and  $I_Z = \pm 3/2$  of the ground state are used as qubit states and are labelled  $|0\rangle$  and  $|1\rangle$  respectively. The reason for choosing hyperfine levels as qubit states is that they have a comparatively long coherence time, about  $500 \mu\text{s}$  at liquid helium temperature [24]. Logical operations are performed by using laser light on the  ${}^3\text{H}_4 - {}^1\text{D}_2$  transition, and different qubits are addressed by using different frequencies of the laser light within the inhomogeneous absorption profile. In the original design, an ensemble approach is used, where all ions that are resonating at a particular frequency are used together as one qubit. Figure 4.3 illustrates this. Since the homogeneous linewidth is of the order of kHz, while the inhomogeneous linewidth is of the order of GHz, a crystal can in principle accommodate millions of qubits. One problem that can

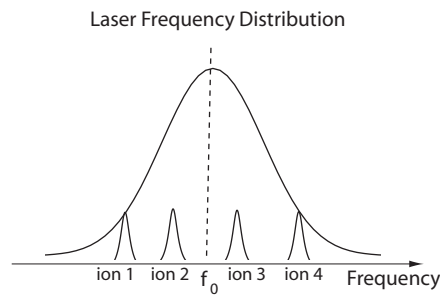


Figure 4.4: Since the spectral width of the laser pulses is significantly broader than the homogeneous linewidth, the pulse will affect a number of ions with slightly different resonance frequency. Ions slightly off-resonance will experience a lower Rabi frequency than ions on the laser center frequency  $f_0$ .

be encountered is that the ions of a qubit do not experience the same light intensity, and thus not the same Rabi frequency. This can be understood by looking

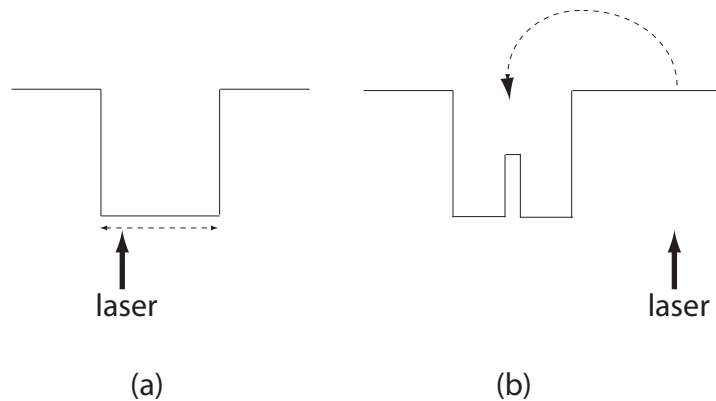


Figure 4.5: (a) The laser is scanned over a part of the inhomogeneous absorption profile, and pumps the ions here to the  $|aux\rangle$  state. This results in a spectral pit, a spectral interval that has essentially no absorption. (b) The laser frequency is shifted, and ions are pumped back into the center of the pit. Now, we have a narrow spectral feature that can be used as a qubit.

at figure 4.4. In this figure, it is clear that the ions sitting at the center frequency experience a higher Rabi frequency than the ions slightly off-resonance. For the scheme to work, it is important that the laser pulses affect all ions of the addressed qubit in the same way, while other ions must not be affected at all. This can be achieved through *spectral holeburning*. In this context, spectral holeburning means deactivating certain ions by pumping them to a state that is not used in the computing scheme. The state in question is the  $I_Z = \pm 5/2$  state, often referred to as  $|aux\rangle$ . The first step of the holeburning process is to pump all ions in a certain interval, typically 10s of MHz wide, to the  $|aux\rangle$  state. This is achieved by scanning the laser repeatedly across this interval. The atoms are then excited to the first excited state. When they relax to the ground state, they have a certain probability of relaxing to the  $|aux\rangle$  state. If they relax to the  $|0\rangle$  or  $|1\rangle$  state, they will be excited again, until eventually, virtually all atoms will be in the  $|aux\rangle$  state. This creates a *spectral pit* in the absorption profile, as the number of absorbers in this interval has been reduced to virtually zero.

Next, the laser frequency is shifted in order to pump ions in a very narrow spectral interval back into the pit. The result is a profile that looks like figure 4.5. The resulting peak is now used as a qubit. Now it is possible to design pulses that affect all ions in the qubit with virtually the same pulse area, and that at the same time do not affect any other ions at all.[19]

## 4.5 Gate Operations in the REQC

As was noted previously, a number of single-qubit operations and one two-qubit operation are sufficient to make a complete set of gates. Single-qubit gates are, at least in theory, straightforward to accomplish. As was described in chapter

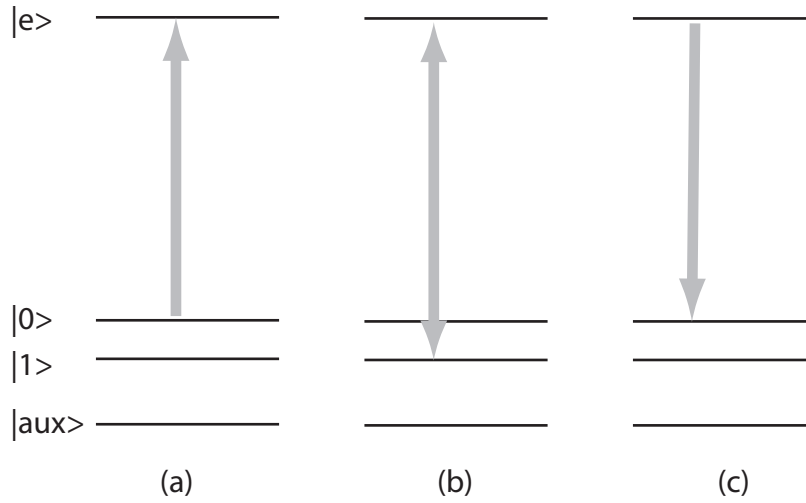


Figure 4.6: A NOT gate. (a) The probability amplitude of  $|0\rangle$  is transferred to  $|e\rangle$ . (b) The probability amplitudes of  $|1\rangle$  and  $|e\rangle$  are swapped. (c) The probability amplitude of  $|e\rangle$  is transferred to  $|0\rangle$ . The net result is a swap between  $|0\rangle$  and  $|1\rangle$ .

3, a suitably designed coherent light pulse can make an arbitrary Bloch vector rotation, and in particular, a  $\pi$ -pulse can make two levels exchange all their probability amplitude. In our case, the state of a qubit is manipulated using the optical transition between the ground state and the first excited state,  ${}^3H_4 - {}^1D_2$ . In the following discussion, we use the  $|0\rangle$  and  $|1\rangle$  levels as well as one of the hyperfine levels of the excited state, designated  $|e\rangle$ . As an example, it will now be shown how to make a NOT operation. For this, three  $\pi$ -pulses tuned to different transitions are used. The first pulse is resonant with the  $|0\rangle - |e\rangle$  transition, and puts all the probability amplitude of  $|0\rangle$  into  $|e\rangle$ . The second pulse is tuned to the  $|1\rangle - |e\rangle$  transition and exchanges all probability amplitude between these two levels. Finally, the third pulse, applied on the same frequency as the first, transfers the amplitude of the excited state to the  $|0\rangle$  state. More formally expressed, the transitions can be written as  $\alpha|0\rangle + \beta|1\rangle \rightarrow \alpha|e\rangle + \beta|1\rangle \rightarrow \alpha|1\rangle + \beta|e\rangle \rightarrow \alpha|1\rangle + \beta|0\rangle$ , which is exactly the definition of a NOT operation. See also figure 4.6.[31]

The realization of two-qubit gates utilizes the fact that the electric dipole moment of an ion changes when the ion is excited. This will shift the resonance frequency of other ions in the vicinity, since they are now subject to a slightly different electric field. To realize a CNOT gate, the following scheme can be used:

1. Apply a  $\pi$ -pulse on the  $|0\rangle - |e\rangle$  transition of the control qubit. If the control qubit is in state  $|0\rangle$ , it will be excited, and this will shift the resonance frequency of surrounding ions, including those representing the target qubit. If the control qubit is in state  $|1\rangle$ , nothing will happen.
2. Perform a NOT operation on the target bit as described above. Note that if the control qubit has been excited, the optical transition of the target

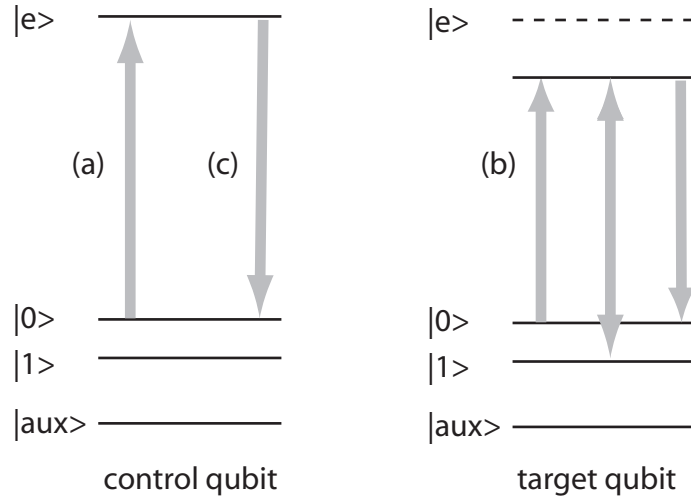


Figure 4.7: A CNOT gate. (a) A  $\pi$  pulse is applied to the control qubit on the  $|0\rangle - |e\rangle$  transition. This will excite the qubit, if it was initially in the  $|0\rangle$  state. (b) A NOT pulse sequence is applied on the target qubit. If the control qubit is in the excited state, the target qubit will have changed its transition frequency, and the NOT sequence will have no effect. (c) The control qubit is brought back to the ground state by a  $\pi$  pulse.

qubit will no longer be on resonance with the incoming light. This means that the NOT operation will only be performed if the control bit has not been excited, i.e. it was initially in the  $|1\rangle$  state.

3. Apply a second  $\pi$ -pulse on the  $|0\rangle - |e\rangle$  transition of the control qubit. This will transfer any probability amplitude in the excited state back to its initial state.

See figure 4.7. Note that all ions of the target qubit must be sufficiently close to an ion of the control qubit so that their resonance frequency becomes shifted when the control qubit is in the excited state. Since it must be possible to apply the CNOT gate to any two qubits, the ions of every qubit must be sufficiently close to ions of other qubits such that CNOT operations can be made with all other qubits either directly or mediated by other ions. The ions that do not couple strongly enough to other ions must be deactivated in the sense that they must be made not to take part in the computations. This can be achieved through a distillation process, described in [32]. Consider two qubits, with resonance frequencies  $\omega_C$  and  $\omega_T$  where you want to remove the ions of each qubit that do not couple strongly to the other ion.

1. Apply a  $\pi$ -pulse on  $\omega_C$ . This will excite the control qubit, which will cause the strongly interacting ions of the target qubit to shift away significantly from  $\omega_T$ .
2. Optically pump the ions on the  $\omega_T$  frequency to the  $|aux\rangle$  state. This will remove all ions that have not had their resonance frequencies significantly shifted.

3. Apply a second  $\pi$ -pulse on  $\omega_C$  to bring the control qubit back to the ground state.
4. Reverse the roles of the two qubits and repeat the procedure.

It has been estimated that given a crystal with a doping concentration of 0.05% and a laser beam exciting ions in a 1 MHz interval in a volume of  $0.004 \text{ mm}^3$  (which are quite typical values), about 0.4% of the ions of two randomly chosen qubits will have sufficient interaction strength [19]. This can cause severe scalability problems; for each qubit that is added to the quantum register, the number of ions per qubit decreases by a factor of  $4 \cdot 10^{-3}$ . The problem with this is that with current readout techniques, it is necessary to have a certain number of ions in order to measure the state of the qubit. One proposition to partly alleviate the problem is to use a bus architecture, where one ion, the *bus ion*, is used to mediate interaction between other ions. In this case, each ion needs to couple only to a bus ion, and not to ions belonging to other qubits [32]. Another proposal is to use a single-ion approach, in which each qubit is represented by only a single ion [33]. This approach makes the readout procedure very challenging, but there are ideas about how to make a sufficiently efficient readout scheme. This is presented in the next section.

## 4.6 Readout

In order to measure the state of a qubit in the ensemble case, there are mainly three methods that have been proposed: Fluorescence, absorption and coherent emission. For the single-ion scheme, another readout mechanism which utilizes a specialized *readout ion* has been proposed. These schemes will be discussed briefly below.

In the fluorescence case, ions are excited either on the  $|0\rangle - |e\rangle$  or the  $|1\rangle - |e\rangle$  transition. The amount of fluorescence emitted from the crystal by this will be proportional to the average probability of finding the ions of that qubit in that state.

In absorption measurements, laser light is sent through the sample at the frequency of the qubit of interest, and the amount of light passing through is measured. The measurement can be greatly improved by using a reference beam to account for amplitude variations of the laser. In this case, the beam is split in two beams: One that propagates through the sample, and one that does not. By dividing the measured intensities of these two beams with each other, an accurate reading of the absorption can be obtained.

For coherent readout, the idea is to create a coherent superposition between one of the ground state levels and the  $|e\rangle$  level. One way to do that is to apply a  $\pi/2$  pulse on the  $|0\rangle - |e\rangle$  transition. This will set up a coherence between  $|1\rangle$  and  $|e\rangle$ , which will cause the ions to emit coherent radiation, as was described in the discussion about free induction decay in section 3.4.2. The amplitude of the emitted light will depend on the level of inversion (with a maximum amplitude for states along the equator of the Bloch sphere), and the phase of the light is determined by the phase of the ions. The phase can be measured by mixing the

emitted light with laser light at a slightly different frequency. This will produce a measurable beating signal.[19]

In order to read out the qubits in the single-ion approach, it is necessary to make a single ion emit a sufficient number of photons per second to produce a measurable signal. In principle, it is possible to produce a large number of photons per ion using fluorescence measurements, in which the ion is repeatedly excited to an optically excited state, which causes it to continuously emit fluorescence light. However, the requirements on ions to make them suitable for readout are substantially different than the requirements for qubit ions. For readout ions, it is important that the ion can not be trapped in a non-fluorescent state, and it must have a large transition strength on the transition of interest. Since a large transition strength leads to shorter coherence times, this requirement is in conflict with the desired properties of qubits. Therefore, it has been proposed to dope a second kind of ion into the crystal, to be used specifically to facilitate readout [33]. To read out a qubit, two laser beams are required; one tuned to the transition frequency of the qubit ion, and one tuned to the transition frequency of the readout ion. The first step is to excite the qubit ion on the  $|0\rangle - |e\rangle$  transition. If the qubit was in state  $|0\rangle$ , it will be optically excited, which will shift the transition frequency of the readout ion out of resonance with the readout beam. The beam tuned to the readout ion frequency is then turned on. This will produce fluorescence light if and only if the readout ion has not been shifted off resonance.

One candidate for a readout system is the 4f-5d transition of the  $\text{Ce}^{3+}$  ion. The lifetime of the 5d state is about 20 ns in  $\text{YPO}_4$ , and the ion has a zero nuclear magnetic moment, which means that there is no hyperfine splitting which could cause the ion to decay to a state where it no longer interacts with the readout beam. However, the properties of  $\text{Ce}^{3+}$  in the  $\text{Y}_2\text{SiO}_5$  host are not well known, and more research needs to be done.[33]

# Chapter 5

## Equipment

### 5.1 The Laser

The laser used for the experiments is a Coherent CR-699-21 ring dye laser, operated in continuous wave (CW) mode and pumped by a Coherent Verdi V-6 diode-pumped, frequency-doubled Nd:YVO<sub>4</sub> laser, with an output wavelength of 532 nm. The dye used was Rhodamine 6G, and the laser was set up for operation at 605 nm. Typical output powers were 3.75 W for the pump laser and 200 mW for the dye laser. The reason for using a dye laser is that it can access any frequency in a wide range with powers of the order of hundreds of mW. However, the gain medium in these lasers consists of a jet of liquid, which is not very stable, and its thickness can vary slightly in time. This changes the optical path length of the laser cavity, which makes it more difficult to keep the laser frequency stable.

The commercial version of the dye laser can be actively frequency-stabilized with a mirror mounted on a piezo-electric crystal inside the cavity, using the transmission fringes of a temperature-stabilized Fabry-Perot etalon as reference. In this way, a linewidth of 1 MHz can be achieved, and the long-term frequency drift is specified at less than 100 MHz/hour [34]. To improve frequency stability, the laser has been equipped with an external stabilization system, in which a Pr<sup>3+</sup>:YSO kept at a few K is used as frequency reference. In order to stabilize the laser, a hole is burned in the inhomogeneous absorption profile, and the light transmission from the crystal can then be used as a frequency reference. In this way, considerable stability improvements have been achieved. Measurements show that the short term linewidth of the system is a few kHz, with a frequency drift which is typically tens of kHz per second. To improve amplitude stability, an amplitude stabilization system with an electro-optic modulator was mounted just after the output coupling mirror of the laser.

## 5.2 Modulators and Modulator Drivers

### 5.2.1 Acousto-Optic Modulators

Acousto-optic modulators (AOMs) were used for two purposes: To create the desired pulse sequences from the CW output of the laser, and to gate the light coming into the detector, to make sure that the excitation pulses were heavily attenuated when reaching the detector, while the echo pulses should be detected with as high sensitivity as possible.

In an AOM, the laser beam passes through a crystal in which a piezo-electric transducer, driven by an external RF source, is being used to transmit an acoustic wave in a direction perpendicular to the beam. The acoustic wave creates a periodic modulation of the refractive index of the crystal. This will distort the wave front of the laser beam, and it can be shown that the light will be diffracted in different orders according to the familiar grating equation:  $m\lambda = d \sin \theta_m$ , where  $m$  is the order of diffraction,  $\lambda$  is the wavelength of the light,  $d$  is the wavelength of the acoustic wave and  $\theta_m$  is the angle of diffraction of the  $m$ :th order.

In addition, the light will change its frequency by an amount  $m \cdot F$ , where  $F$  is the frequency of the acoustic wave. This can be intuitively understood by viewing the diffraction as a process in which the light photon absorbs or emits the energy of one or more phonons. Furthermore, the phase of the light is also shifted by an amount that depends on the phase of the acoustic wave. The intensity of the diffracted light depends on the intensity of the acoustic wave.

One must also consider that in a thick crystal, light can be diffracted at different depths. To get strong light in a particular order, the crystal must be aligned so that light diffracted at different depths interfere constructively. Thus, it is possible to align the crystal to maximize power in a particular order. Normally, the first order of the diffracted light is used as output of the modulator. Other orders can be removed by placing an iris after the AOM.[35]

The most versatile way to control an AOM is to use an arbitrary waveform generator (AWG) to generate the RF signals to the piezoelectric transducer. This makes it possible to create arbitrary pulse sequences in which both pulse durations and pulse shapes, including intensity, frequency and phase, can be controlled. In the experiments presented in this thesis, the pulses were generated by an AOM with a center frequency of 200 MHz, driven by a Tektronix AWG520 AWG, which in turn was controlled by an ordinary PC.

Two Isomet 1205C AOMs with a center frequency of 80 MHz and a bandwidth of 30 MHz were used for *gating*. The concept of gating is to let light into the detector *only* when the signal of interest (in this case the echo) is expected. In this case, it is only necessary to be able to switch the light on and off. The gating AOMs were driven using an Isomet D320 driver unit containing a voltage-controlled oscillator (VCO), which was switched on and off by a TTL signal from the AWG.

## 5.2.2 Electro-Optic Modulators

Electro-optical modulators (EOMs) consist of a material which changes its refractive index when a voltage is applied across it. This is known as the *electro-optic effect*. If the crystal is properly oriented, the applied voltage can induce birefringence, which rotates the polarization of the incoming light. By putting a polarizer after the EOM, it is possible to control the amount of light being transmitted.[19] In this work, an EOM was used to stabilize the amplitude of the laser.

## 5.3 The Cryostat

To keep the sample at cryogenic temperatures, and to produce the magnetic fields necessary for the experiments, an Oxford Instruments Spectromag cryostat was used. The cryostat consists of:

1. An *Outer Vacuum Chamber* (OVC), which is used to prevent heat conduction from the outside environment to the inner parts of the cryostat. The OVC is kept at high vacuum, typically around  $10^{-6}$  mbar or lower.
2. A helium reservoir, which contains up to 20 l of liquid helium, which keeps the reservoir at 4.2 K. The helium reservoir is mounted inside the OVC.
3. A nitrogen jacket, which contains liquid nitrogen at 77 K. The jacket is a ring-shaped container which is mounted in the OVC and surrounds the helium reservoir. Its role is to reduce the heat load on the helium reservoir by thermal radiation. Since the amount of heat radiated from an object is proportional to the temperature raised to the power of 4, it makes a very big difference that the helium reservoir is surrounded by an object at 77 K instead of being directly exposed to the room temperature surroundings at 300 K.
4. A superconducting magnet, rated up to 7 T for operation at 4.2 K, and up to 8 T at 2.2 K. The magnet is mounted in the bottom of the helium reservoir, and is in this way always immersed in liquid helium as long as the helium reservoir is not empty.
5. A *Variable Temperature Insert* (VTI), which contains the sample itself. The VTI is placed in the middle of the magnet bore, but has no direct contact with the helium reservoir. This makes it possible to control the temperature of the sample independently of the temperature of the magnet. The VTI can be kept at low temperature with the help of helium, which is transferred to the VTI from the helium reservoir through a small capillary tube, in which the flow of helium is controlled by a motorized needle valve. Normally, an externally connected vacuum pump is used to promote the helium flow through the VTI. The VTI also contains a heater, which makes it possible to keep the sample at as high temperature as 300 K. However, for the experiments conducted here, the sample was always kept at a few K. The sample is mounted at the end of a sample rod, which is loaded from the top of the cryostat. This arrangement makes it possible

to adjust the position and orientation of the sample, as well as to change samples, even when the cryostat is at liquid helium temperature.

6. A *Lambda Point Fridge* (LPF), mounted inside the helium reservoir. This device can be used to lower the temperature in the lower part of the helium reservoir to 2.2 K, which allows the magnet to be run up to 8 T. The LPF consists of a small chamber which can be connected to an external vacuum pump, and has a needle valve which can be opened to let in helium from the reservoir. By letting helium into the LPF chamber and using the vacuum pump to lower the pressure inside, the temperature of the helium will drop. This will cool down the LPF, which in its turn lowers the temperature of the helium of the reservoir surrounding the LPF. Since the density of the liquid increases as it is being cooled, strong convection currents will be set up between the LPF and the part of the reservoir below it, where the magnet is installed. The benefits of the system is that only the liquid in the immediate vicinity of the magnet is cooled, which minimizes the helium evaporation rate.[36]

A more detailed description can be found in [37]. A very large portion of the work was devoted to putting the cryostat into operation. Because of this, a much more detailed discussion about how the cryostat works and how to operate it has been written and can be found in appendix B. It is written mainly as a help to other people working with the cryostat.

## 5.4 Detectors

To detect light from the experiments, both *photodiodes* and *photomultiplier tubes* have been used. A photodiode is a diode which produces a current when it is being hit by light. A photodiode can be operated in either zero-bias or reverse-bias mode. When operating in zero-bias mode, it makes use of the *photovoltaic effect*, which works as follows: Incident light creates electron-hole pairs. When freed electrons on the *n* side of the diode recombine with holes from the *p* side and vice versa, the electric field inside the diode will change, which causes a voltage to be developed across the diode. In reverse-bias mode, a voltage is applied in the reverse direction over the p-n junction. Normally, a reverse-biased diode has a very high resistance, but incident light will cause this resistance to decrease, which produces a measurable signal.[38] In the experiments, the photodiodes have been operated in reverse-bias mode, since this increases the sensitivity of the diodes. They have been used to measure strong signals such as the excitation pulses.

A photomultiplier tube (PMT) is an evacuated tube that contains a photosensitive material, known as the *photocathode*, and a number of electrodes known as *dynodes*. Incident light hits the photocathode, which emits electrons through the photo-electric effect. These electrons are accelerated by a voltage between the photocathode and the first dynode. When the electron hits the dynode, a number of secondary electrons are emitted, which are accelerated towards the second dynode. After a number of dynodes, the electrons hit an anode, and the current produced in this way can be measured and displayed on an oscilloscope.

Typically, a photomultiplier tube has of the order of ten dynodes and operates at a voltage across the whole dynode chain of 1-2 kV. A photomultiplier tube is characterized by very high gain, low noise and short rise times.[39] In the experiments, a photomultiplier tube was used to measure the photon echoes, which were too weak to be measured by a photodiode.



## Chapter 6

# Experiment and Results

The aim of the experiment was to measure the optical coherence time of the  ${}^3\text{H}_4-{}^1\text{D}_2$  transition in  $\text{Pr}^{3+}:\text{Y}_2\text{SiO}_5$  as a function of magnetic field strength. This was done using two-pulse photon echoes. The coherence time was measured for four magnetic field strengths: 0 T, 0.01 T, 0.1 T and 1 T.

### 6.1 Experimental setup

The setup was divided into two parts, set on two optical tables. The first part, shown in figure 6.1, was used to create the excitation pulses used in the experiment, and consisted of:

- The pump laser and the dye laser.
- The frequency and amplitude stabilization system for the laser. This included an EOM used to regulate the amplitude, and a continuous flow type liquid helium cooled cryostat (Oxford Instruments Optistat) containing a  $\text{Pr}^{3+}:\text{Y}_2\text{SiO}_5$  crystal used to provide a reference for the frequency locking system.
- A 200 MHz AOM. The AOM was mounted in a double-pass configuration, which made it possible to change the frequency without causing any beam movement, and also to achieve a higher bandwidth than would be possible using a single-pass configuration. The signals for the AOM were generated by a Tektronix AWG520 arbitrary waveform generator, controlled by a computer.
- A single-mode optical fibre to transmit the pulses to the other part of the setup. The reason for using a fibre to transmit the pulses between the tables was because if the beam had been sent through open air, movements of the tables would have resulted in poor phase stability and would have caused the beam to move.

The other part of the setup, shown in figure 6.2, consisted of the sample itself, mounted inside the Spectromag cryostat, and various detectors. The sample

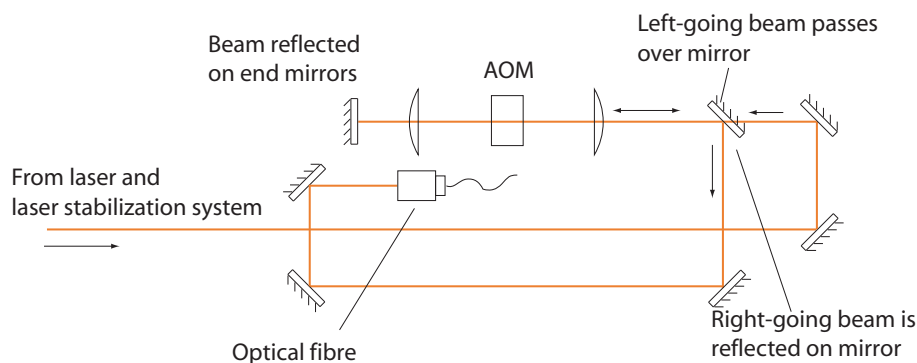


Figure 6.1: *The pulse shaping setup. The AOM is arranged in a double-pass configuration, in which the light passes through the AOM in one direction, is reflected and then passes through in the opposite direction. In this way, the modulator is used twice, effectively doubling the bandwidth and eliminating beam movements.*

was a  $\text{Pr}^{3+}\text{Y}_2\text{SiO}_5$  crystal with a doping concentration of 0.005%. It had the dimensions  $4 \times 5 \times 6$  mm, with the b axis normal to the  $5 \times 6$  mm surface, the D1 axis normal to the  $4 \times 6$  mm surface and the D2 axis normal to the  $4 \times 5$  mm surface. The light from the fibre had a beam diameter of approximately 4 mm and was focused into the sample by a lens with a focal length of 30 cm. This should theoretically make a focus with a beam diameter of approximately  $60 \mu\text{m}$ . The beam diameter was measured with the help of a razor blade mounted on a translation stage. The micrometer screws of the translation stage were used to move the blade across the beam, and a photodiode was used to measure the transmitted intensity as a function of razor blade position. In this way, a focus diameter of  $100 \mu\text{m}$  was measured, and this value has been used in subsequent calculations.

A few percent of the light was removed from the beam by a beam pick-off and was focused into a photodiode, to provide a reference measurement of the intensity of the excitation pulses. The light passing through the sample was directed through two 80 MHz gating AOMs and focused into a Hamamatsu R943-02 photomultiplier tube, which was used to detect the echoes. It is necessary to use gated measurements since the excitation pulses are generally much stronger than the echo pulse. Letting the excitation pulses into the PMT could have caused saturation, or even permanent damage to the PMT. The 0:th order of the light from the first AOM was directed by a mirror into a second photodiode to provide a measurement of the intensity of the excitation pulses after having passed through the sample. The signals from the photodiodes and the photomultiplier were digitized and recorded by a LeCroy Waverunner 6050A digital oscilloscope.

## 6.2 Experiments

For each value of the magnetic field being measured, 6 series of measurements were made using different excitation intensities. The reason for doing this was

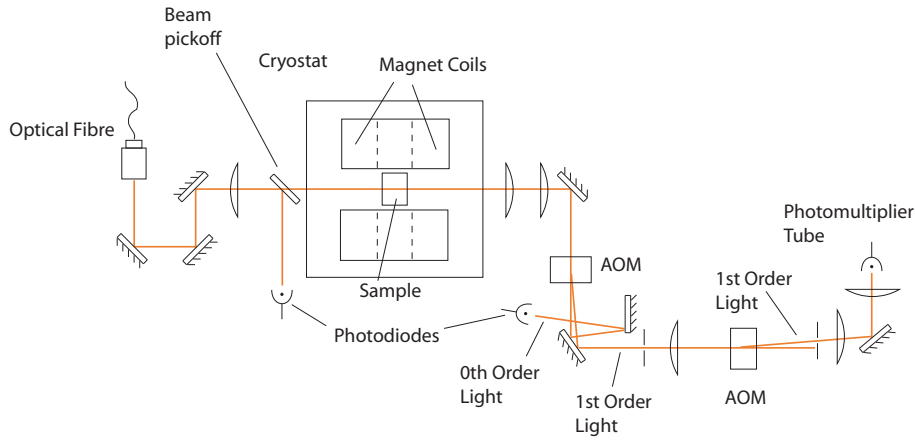


Figure 6.2: *The setup on the Spectromag table, showing the Spectromag itself as well as the detector setup.*

to be able to compensate for the effect of instantaneous spectral diffusion on the coherence times, as discussed in section 4.3. By measuring the linewidth as a function of excitation density (the number of excited ions per volume unit), it should be possible to obtain the linewidth at zero excitation density through extrapolation.

For each excitation intensity, the magnitude of the echo was measured for 33 different time separations between the excitation pulses: From  $4 \mu\text{s}$  to  $102 \mu\text{s}$  in steps of  $3 \mu\text{s}$ . Each of these time separations were measured 20 times. In all cases, the excitation pulses were gaussian, with a full width half maximum (FWHM) of  $0.8 \mu\text{s}$ . After each measurement, the laser was repeatedly scanned across several tens of MHz for 100 ms, to erase any spectral gratings that might form and to make sure that the population was in an equilibrium-like state at the beginning of each measurement. The pulse sequence is described in greater detail in appendix A. A delay of 200 ms was made after each measurement to make sure that the erase sequences did not heat the sample. For the same reason, the measurements were made with the sample immersed in liquid helium rather than helium gas, to achieve greater cooling power. The pressure above the liquid helium was lowered by a vacuum pump to keep the helium temperature at 2 K. It was deemed necessary to keep the temperature below 2.2 K at all times when cooling with liquid helium, since above this point the measurements are heavily influenced by bubbles forming in the helium. Light was sent through the sample along the b-axis, with the polarization along D2. The magnetic field was parallel to the D1 axis.

To obtain a measurement of the amount of light being absorbed in the sample, calibration curves were measured for the two photodiodes, which provided a relation between the signal measured by the photodiodes and the actual power of the light just before and just after the cryostat. This calibration was converted to a relationship between the measured area of a pulse and the energy content of the pulse. The power was then measured just before and just after the cryostat with the laser tuned off resonance to obtain a measurement of how much light

is lost through reflections on the windows of the cryostat and on the crystal surfaces. This information made it possible to calculate the amount of light being absorbed by the dopant ions, and thus the number of ions that were excited, in the following way:

When the light enters the cryostat, it passes through five surfaces, including the crystal surface itself, and some light is lost through reflections. Next, some light is lost through absorption by the dopant ion. Finally, the light passes through an additional five surfaces on its way out. When measuring the intensity off resonance, losses arise only from surface reflections. It is reasonable to assume that the absorption is the same before and after the crystal. Thus, the transmittance for five surfaces,  $T$ , can be estimated by inserting the measured power before the cryostat  $P_{\text{before}}$  and the power after the cryostat  $P_{\text{after}}$  into:

$$P_{\text{after}} = T^2 \cdot P_{\text{before}} \quad (6.1)$$

This gave a value of  $T$  of 0.80. Now, when an excitation pulse was sent through the sample on resonance, the energy reaching the sample was given by  $T \cdot E_{\text{before}}$ , where  $E_{\text{before}}$  is the energy of the pulse before it enters the cryostat. A certain amount of the light,  $E_{\text{abs}}$ , was absorbed by the ions. This light was further attenuated by a factor of  $T$  through surface reflections on its way out. The amount of light measured after the cryostat,  $E_{\text{after}}$ , was given by  $E_{\text{after}} = T \cdot (T \cdot E_{\text{before}} - E_{\text{abs}})$ . Thus, the amount of absorbed light energy was given by:

$$E_{\text{abs}} = T \cdot E_{\text{before}} - \frac{E_{\text{after}}}{T} \quad (6.2)$$

The excitation density  $n_e$  is given by

$$n_e = \frac{E_{\text{abs}}}{E_{\text{photon}} \cdot A \cdot l} \quad (6.3)$$

where  $E_{\text{photon}}$  is the energy of one photon,  $A$  is the beam area inside the sample and  $l$  is the thickness of the sample. In addition, the actual excitation pulse sequence consisted of two pulses, the first having an intensity of 1/4 of that of the second one. The value of  $n_e$ , measured using only one pulse, was therefore multiplied by a factor of 5/4.

### 6.3 Data Evaluation

*“If you need statistics, you did the wrong experiment.”*

–Attributed to Ernest Rutherford

For each magnetic field strength and excitation density, the echo intensities were averaged over the 20 measurements that were made for each pulse separation time. This average was plotted as a function of pulse separation. An exponential decay curve was fitted to each of these plots according to:

$$f(t) = I_0 e^{-4t/T_2} + I_b \quad (6.4)$$

where  $I_0$  is the echo intensity at zero pulse separation,  $t$  is the separation time and  $I_b$  is the background intensity. The parameters  $I_0$ ,  $T_2$  and  $I_b$  were determined using a weighted least squares-fit, that is finding the values of these

parameters which minimize:

$$Q^2 = \sum_i W_i (I_i - f(t_i))^2 \quad (6.5)$$

where  $I_i$  is the value of data point  $i$ ,  $t_i$  is the pulse separation time at data point  $i$  and  $W_i$  is the fitting weight at data point  $i$ . The weights were chosen as:

$$W_i = \frac{1}{\sigma_i^2} \quad (6.6)$$

where  $\sigma_i$  is the estimated standard deviation of data point  $i$ . Since each data point is a mean of 20 measurements, the standard deviation can be estimated by:

$$\sigma_i = \frac{1}{\sqrt{20}} \cdot \left( \frac{1}{n-1} \sum_{k=1}^n (t_{ik} - \bar{t}_{ik})^2 \right)^{1/2} \quad (6.7)$$

The expression to the right is the usual formula for calculating the standard deviation of measurements, divided by  $\sqrt{20}$  to get the standard deviation of the mean of twenty such measurements. The linewidth was then calculated from the value  $T_2$  determined by the process above and plotted as a function of excitation density for each magnetic field. To make error estimates, the

$\nu$	F(1, $\nu$ ,0.683)
1	3.3837
2	1.7488
3	1.4347
4	1.3052
5	1.2350
6	1.1910
7	1.1609
8	1.1390
9	1.1224
10	1.1094
12	1.0902
14	1.0768
16	1.0669
18	1.0593
20	1.0533
25	1.0426
30	1.0355
35	1.0305
40	1.0268

Table 6.1: Values of the  $F$  function.  $\nu$  is the number of degrees of freedom.

procedure described in section 4.8 in [40] was used. The idea is vary  $T_2$  around the value determined by the least-squares fit, while the other two parameters remain fixed, and to plot the quantity  $Q^2$  as a function of this  $T_2$ .  $T_2$  has obviously its minimum at the value determined by the least-squared fit, as this is the definition of the best fit. The plot  $Q^2$  vs.  $T_2$  has a near-parabolic shape

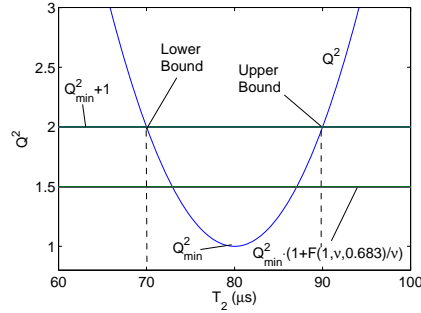


Figure 6.3: Example of a  $Q^2$  vs.  $T_2$  plot used to determine the uncertainties of the fit. The curve resembles a parabola around the minimum value. The upper and lower  $1\sigma$  bounds are given by the  $T_2$  values of the points where the  $Q^2$  curve intersects the greater of the quantities  $Q_{\min}^2 + 1$  and  $Q_{\min}^2 \cdot (1 + F(1, \nu, 0.683)/\nu)$ .

for a reasonably linear problem. The upper and lower  $1\sigma$  bounds (one standard deviation) are given by the values of  $T_2$  at the two points around  $Q_{\min}^2$  where  $Q^2$  intersects the larger of the quantities  $Q_{\min}^2 + 1$  and  $Q_{\min}^2 \cdot (1 + F(1, \nu, 0.683)/\nu)$ . Here,  $\nu$  is the number of degrees of freedom,  $\nu = N - (n - 1)$ , where  $N$  is the number of data points and  $n$  is the number of fitted parameters, and  $F$  is a function whose values are shown in table 6.1. An illustration of what such a plot can look like is given in figure 6.3. In this experiment,  $Q^2 + 1$  has always been the greater value, due to the large number of data points.

## 6.4 Results

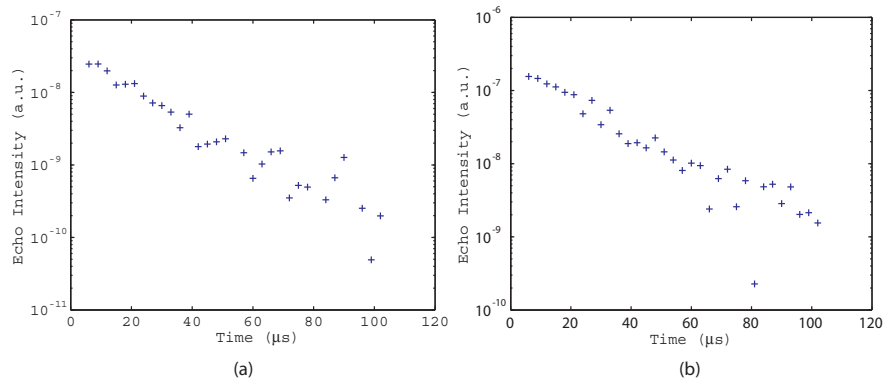


Figure 6.4: Two typical plots of echo intensity versus pulse separation time, shown in log scale. The estimated background intensities have been subtracted from the plots. (a) shows a curve for zero magnetic field and an excitation density of  $2.2 \cdot 10^{17}$  ions /  $m^3$ . (b) shows a curve for a magnetic field of 1 T and an excitation density of  $1.4 \cdot 10^{19}$  ions /  $m^3$ .

A couple of representative decay curves, with the fitted background intensity subtracted, are shown in figure 6.4. It can be seen that they correspond well to exponential curves. However, a few of these curves showed a slight periodic modulation in addition to the exponential decay, with a period time of approximately 15–20  $\mu\text{s}$ .

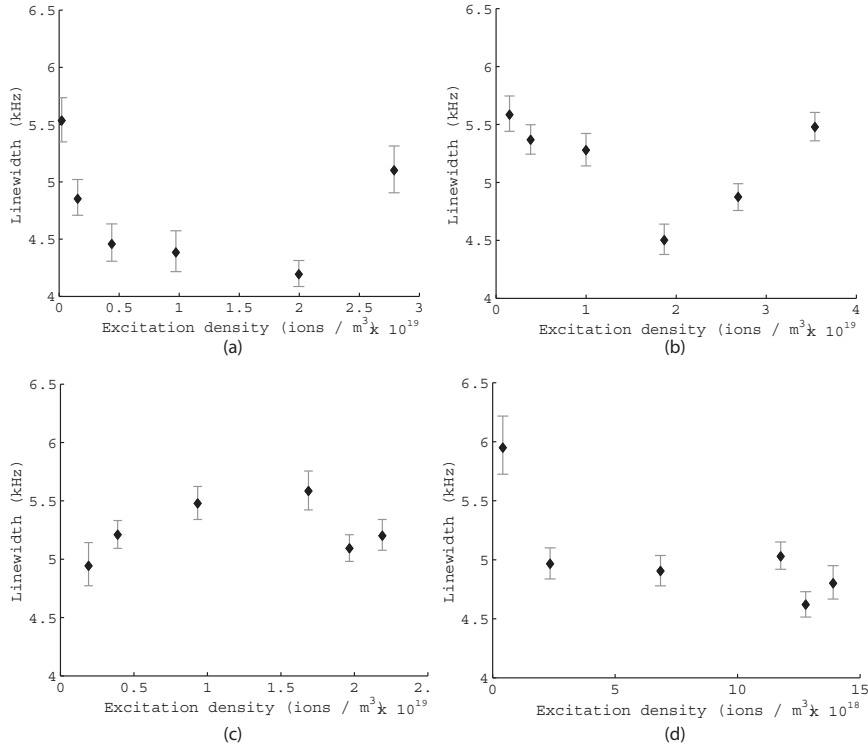


Figure 6.5: *Linewidths versus excitation density for (a) 0 T (b) 0.01 T (c) 0.1 T and (d) 1 T. No clear connection can be established between the linewidth and the excitation density. Also, the presence of magnetic fields does not seem to affect the linewidths in a clearly visible way.*

Figure 6.5 shows the final result, where the linewidth is plotted as a function of excitation density for all four magnetic fields, along with error estimates. In all cases, the results are around 5 kHz, but the variations are large. The narrowest linewidth was  $4.20^{(+0.12)}_{(-0.11)}$  kHz, and the broadest linewidth was  $5.95^{(+0.27)}_{(-0.23)}$  kHz, corresponding to coherence times of  $75.9^{(+2.1)}_{(-2.1)}$   $\mu\text{s}$  and  $53.5^{(+2.2)}_{(-2.3)}$   $\mu\text{s}$  respectively.

The background intensity  $I_b$  that was estimated by the curve fitting procedure is shown in figure 6.6.

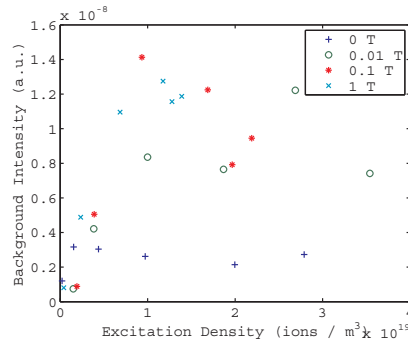


Figure 6.6: *Background intensity, estimated using the procedure described in section 6.3. Note that the background values are considerably higher for non-zero magnetic fields. It is also evident that the background is significantly smaller at low excitation densities. No satisfactory explanation has been found for either of these observations.*

## 6.5 Discussion

Generally, the reported linewidths are considerably larger than those reported by previous investigations. Equall, Cone and Macfarlane have reported linewidths of 2.4 kHz for zero magnetic field, and 1.9 kHz for a 77 G magnetic field [20]. It remains to be explained whether this discrepancy is due to an experimental artifact or if there is any additional mechanism that is causing dephasing in the present experiments.

No clear dependence of the measured linewidth on the excitation density can be established. However, the excitation densities have generally turned out to be very low, given the excitation intensities involved and the doping concentration of the sample. The excitation density was approximately one order of magnitude lower than those used by Equall, Cone and Macfarlane. Therefore, it seems reasonable to conclude that spectral diffusion did not give a significant contribution to the linewidth in this experiment. One possible explanation for the low excitation density is that the experiment was perhaps not carried out at the center frequency of the absorption profile.

After the initial cryostat tests, it was found that the sample had cracked, because the crystal holder had contracted when it was cooled to liquid helium temperature, which made it exert a very high pressure on the crystal. In the subsequent experiments, care was taken to mount the crystal more loosely, but even so, it is possible that it was subject to severe strain. This could have broadened the inhomogeneous absorption profile, reducing the number of absorbers at the laser frequency. If so, it could be another explanation for the low excitation density.

It is surprising that the measured linewidths for a given magnetic field vary so much and in such a seemingly random manner. As can be seen in figure 6.5, the experimental inaccuracies do not seem to account for these variations. Instead, there might be a systematic error in the measurements. Presently, there are no

satisfactory theories about what these errors could be. Since the variations are so large for a given magnetic field, it is very difficult to make any conclusions about the magnetic field dependence. Previous investigations show that a weak magnetic field lowers the linewidth by 500 Hz, and this value is comparable to the variations of the measured values for each magnetic field strength. Considerably stronger fields did not show no clear impact on the results either.

One suggestion is that there might be a problem that the crystal holder is made of copper instead of a non-metallic material. This could possibly affect the magnetic field experienced by the crystal.

It is well known that ions doped into a noncrystalline host such as glass have significantly shorter coherence times than those of ions in crystals. This can be explained with that in these nonperiodic hosts, the ions can have two close-lying states, which they can tunnel between. These fluctuating states can greatly reduce coherence times. The theory of these tunnelling states is discussed in general in [41] and described in the context of doped glasses in [42]. Since the crystal was subject to such high stress, it is a possible, although perhaps remote, scenario that it has become disorganized enough to accommodate tunnelling states.

It might also be worthwhile to investigate whether the erase pulses could have heated the crystal locally to a temperature significantly above liquid helium temperature. There might be some support for that hypothesis: In an early measurement, the measured linewidths were somewhat narrower than the ones on the measurements in figure 6.5. The measurement was discarded for the following reasons:

- The statistical uncertainties were probably very large, since in these experiments, only one measurement was made for each data point, in contrast to the twenty measurements made in 6.5. The reason for this was that due to limitations of the oscilloscope used, each two-pulse echo sequence had to be loaded into the AWG separately, a process that took approximately ten seconds. This made it impractical to make 660 measurements for a single magnetic field strength and excitation density.
- The statistical uncertainties could not be estimated; since only one measurement was made for each data point, it was impossible to calculate the variance of each data point.
- No accurate estimation of the excitation density could be done. Considerably stronger excitation intensities were used in this experiment than in the one presented in figure 6.5. After the measurements, it was found that saturation effects in the crystal had been significant. This made the reference pulses used to estimate the absorbed energy highly inaccurate.

The results of the measurement are shown in figure 6.7. Not much conclusions can be drawn from them for the reasons mentioned above. However, the measured linewidths are generally narrower than in 6.5, and the only two obvious differences between these measurements and the measurements of figure 6.5 are that the excitation intensities in this case were higher (which hardly could have lowered the linewidth) and that the time between measurements were much greater ( $\sim 10$  s as opposed to 300 ms). This reduced the heat load on the crystal by the laser by two orders of magnitude.

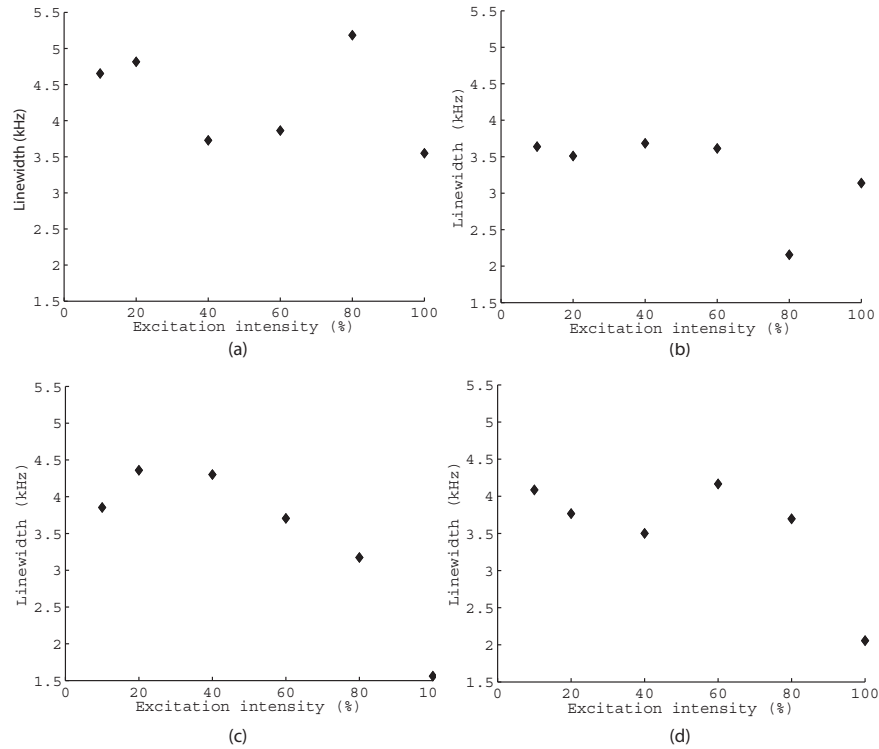


Figure 6.7: *Linewidths versus excitation intensity in an early measurement series for (a) 0 T (b) 0.01 T (c) 0.1 T and (d) 1 T. The average linewidth is somewhat lower than for the linewidths in figure 6.5, but the experimental uncertainties are probably large. Since it was not possible to make an accurate estimate of the excitation density, the horizontal axes show the incident intensity on the crystal, measured as a percentage of the maximum output intensity of the pulse generation system.*

It is a rather surprising result that the background intensity increased by such a large amount when the magnetic field was applied. The process behind this phenomenon is not known. It should be noted, however, that the curve fitting procedure assumes that the curve shape consists of an exponential decay term and a constant background. This is a reasonable assumption, but should it prove to be false, the estimated values of coherence time and background are not valid. As previously mentioned, a slight modulation could be observed in some of the decay curves. Another explanation to the anomalous background levels could be that the detector is affected by the magnetic field. However, this seems unlikely, as the effect is significant even at very low magnetic fields. When the field in the sample was 0.01 T, the field at the PMT should be no more than a few  $\mu\text{T}$ .

## Chapter 7

# Conclusions and Outlook

The measured coherence time of the optical transition  ${}^3\text{H}_4-{}^1\text{D}_2$  was considerably shorter than previously reported,  $\sim 60 \mu\text{s}$  as opposed to  $150 \mu\text{s}$ , and showed no obvious magnetic field dependence. However, it should be noted that there are large and seemingly random variations in the data, larger than can be explained by statistical uncertainties. It seems necessary to find out the reasons for the short coherence times. If the measured coherence time in any way is limited by additional dephasing mechanisms, or limitations in the experimental setup or the techniques used, this must be understood in order to eliminate such effects in future measurements. Sufficiently long coherence times are necessary in order to implement efficient quantum gates. A complex gate may require several pulses and have a duration of several  $\mu\text{s}$ . The probability of coherence loss during this time must be very small in order to achieve a high gate operation fidelity.

Furthermore, in all measurements, the magnetic field was oriented along the D1 axis. To obtain comprehensive data of magnetic field dependence of coherence times, a variety of orientations should be tested.

Finally, it is of major interest to measure the coherence times between the hyperfine levels in the ground state. This was originally a major objective of this thesis, but had to be abandoned due to time constraints.



## Chapter 8

# Acknowledgements

First of all, I would like to thank my supervisor Brian Julsgaard and my co-supervisor Stefan Kröll for all the time they have spent discussing ideas with me, helping me with troubleshooting, helping me with interpreting results, helping me with the laboratory work, reading my manuscript, and generally for making this work possible at all. I would also like to thank Lars Rippe, who spent much more time helping me than I had the right to ask for, for all support, both technical and moral. Additionally I would like to thank all who worked in the Photon Echo Group during my stay: The people mentioned above as well as Atia Amari, Julio Hernández, Johan Tholén and Andreas Walther, for providing such a nice atmosphere, which made my stay so pleasant, in spite of all frustrations.

The cryostat would never have been put in working order without Leif Magnusson at Kryolab and Andreas Fuhrer at the Solid State Physics division, who sacrificed a lot of time to help me, much more than they were obliged to. Furthermore, the fact that Andreas Fuhrer and Ruisheng Liu were willing to lend their helium transfer tube made all the difference between success and total failure.

I would also like to thank my fellow diploma students at the division and all other people who have provided support, and who have patiently listened to all my complaining.

A special thanks to the support engineers of Oxford Instruments Ltd. for their, with some notable exception, limitless patience with all questions.



# Bibliography

- [1] R. Feynman, *Simulating Physics with Computers*, Int. J. Theor. Phys. **21**, 467–488, 1982
- [2] D. Deutsch, *Quantum Theory, the Church-Turing Principle and the Universal Quantum Computer*, Proc. R. Soc. Lond. A **400**, 97–117, 1985
- [3] P. E. Shor, *Polynomial-Time Algorithms for Prime Factorization and Discrete Logarithms on a Quantum Computer*, SIAM J. Comput. **26**, 1484–1509, 1997
- [4] C. J. Foot, *Atomic Physics*, Oxford University Press, Oxford, 2005
- [5] A. Barenco, C. H. Bennett, R. Cleve, D. P. DiVincenzo, N. Margolus, P. Shor, T. Sleator, J. Smolin, H. Weinfurter, *Elementary gates for quantum computation*, Phys. Rev. A **52**, 3457–3467, 1995
- [6] W. Diffie, M. E. Hellman, *New Directions in Cryptography*, IEEE Trans. Inform. Theory **22**, 644–654, 1976
- [7] L. K. Grover, *Quantum Mechanics helps in searching for a needle in a haystack*, Phys. Rev. Lett. **79**, 325–328, 1997
- [8] A. Steane, *Quantum Computing and Error Correction*, In P. E. A. Turchi and A. Gonis, editors, *Decoherence and its implications in quantum computation and information transfer*, volume 182 of *NATO Science Series: Computer & Systems Sciences*, pages 284–298. IOS Press, Amsterdam, 2001
- [9] D. P. DiVincenzo, *The Physical Implementation of Quantum Computation*, Fortschr. Phys. **48**, 771–783, 2000
- [10] J. I. Cirac, P. Zoller, *Quantum Computations with Cold Trapped Ions*, Phys. Rev. Lett. **74**, 4091–4094, 1995
- [11] N. A. Gershenfeld, I. L. Chuang, *Bulk Spin-Resonance Quantum Computation*, Science **275**, 350–356, 1997
- [12] L. M. K. Vandersypen, M. Steffen, G. Breyta, C. S. Yannoni, M. H. Sherwood, I. L. Chuang, *Experimental realization of Shor’s quantum factoring algorithm using nuclear magnetic resonance*, Nature **414**, 883–887, 2001
- [13] D. Loss, D. P. DiVincenzo, *Quantum computation with quantum dots*, Phys. Rev. A **57**, 120–126, 1997

- 
- [14] V. Giovannetti, D. Vitali, P. Tombesi, A. Ekert, *Scalable quantum computation with cavity QED systems*, Phys. Rev. A **62**, 032306, 2000
- [15] Y. Makhlin, G. Schön, A. Shnirman, *Josephson Junction Qubits with Controlled Couplings*, Nature **398**, 305–307, 1999
- [16] M. I. Dykman, P. M. Platzman, *Quantum Computing Using Electrons Floating on Liquid Helium*, Fortscr. Phys. **48**, 1095–1108, 2000
- [17] M. N. Leuenberger, D. Loss, *Quantum computing in molecular magnets*, Nature **410**, 789–793, 2001
- [18] W. Harneit, *Fullerene-based electron-spin quantum computer*, Phys. Rev. A **65**, 032322, 2002
- [19] M. Nilsson, *Coherent Interactions in Rare-Earth-Ion-Doped Crystals for Applications in Quantum Information Science*, Doctoral Thesis, Department of Physics, LTH, **LRAP-333**, 2004
- [20] R. W. Equall, R. L. Cone, R. M. Macfarlane, *Homogeneous broadening and hyperfine structure of optical transitions in  $Pr^{3+}:Y_2SiO_5$* , Phys. Rev. B **52**, 3963–3969, 1995
- [21] T. Böttger, C. W. Thiel, Y. Sun, R. L. Cone, *Optical decoherence and spectral diffusion at  $1.5\ \mu\text{m}$  in  $Er^{3+}:Y_2SiO_5$  versus magnetic field, temperature, and  $Er^{3+}$  concentration*, Phys. Rev. B **73**, 075101, 2006
- [22] C. Li, C. Wyon, R. Moncorge, *Spectroscopic properties and fluorescence dynamics of  $Er^{3+}$  and  $Yb^{3+}$  in  $Y_2SiO_5$* , IEEE J. Quant. Elec. **28**, 1209, 1992
- [23] A. Alexander, *Investigation of Qubit Isolation in a Rare-Earth Quantum Computer*, Honours thesis, Research School of Physical Sciences and Engineering, Australian National University, 2002
- [24] F. Vestin, *Spin Coherence Excitation in  $Pr^{3+}:Y_2SiO_5$* , Master Thesis, Department of Physics, LTH, **LRAP-297**, 2003
- [25] S. Svanberg, *Atomic and Molecular Spectroscopy. Basic Aspects and Practical Applications. 4th ed.* Springer-Verlag, 2004
- [26] F. R. Graf, A. Renn, G. Zumofen, U. P. Wild, *Photon-echo attenuation by dynamical processes in rare-earth-ion-doped crystals*, Phys. Rev. B **58**, 5462–5478, 1998
- [27] R. M. Macfarlane, R. M. Shelby, *Coherent Transient and Holeburning Spectroscopy of Rare Earth Ions in Solids*, in A. A. Kaplyanskii and R. M. Macfarlane (Eds.), *Spectroscopy of Solids*, North-Holland, Amsterdam, 1987
- [28] G. M. Wang, R. W. Equall, R. L. Cone, M. J. M. Leask, K. W. Godfrey, F. R. Wondre, *Optical dephasing mechanisms in  $Tm^{3+}:Y_2Si_2O_7$* , Opt. Lett. **21**, 818, 1996
- [29] E. Fraval, M. J. Sellars, J. J. Longdell, *Method of Extending Hyperfine Coherence Times in  $Pr^{3+}:Y_2SiO_5$* , Phys. Rev. Lett. **92**, 077601, 2004

- [30] M. J. Sellars, E. Fraval, J. J. Longdell, *Investigation of static electric dipole-dipole coupling induced optical inhomogeneous broadening in  $\text{Eu}^{3+}:\text{Y}_2\text{SiO}_5$* , J. Lumin. **107**, 150–154, 2004
- [31] L. Rippe, M. Nilsson, R. Klieber, D. Suter, S. Kröll, *Experimental demonstration of efficient and selective population transfer and qubit distillation in a rare-earth-ion-doped crystal*, Phys. Rev. A **71**, 062328, 2005
- [32] J. Wesenberg, K. Mølmer, *Robust quantum gates and a bus architecture for quantum computing with rare-earth-ion doped crystals*, Phys. Rev. A **68**, 012320, 2003
- [33] J. Wesenberg, K. Mølmer, L. Rippe, S. Kröll, *Scalable designs for quantum computing with rare-earth-ion-doped crystals*, Quant-ph/**0601141**, 2006
- [34] Coherent Inc., *Coherent 699-21 ring dye laser manual*.
- [35] F. L. Pedrotti S. J., L. S. Pedrotti, *Introduction to Optics, Second Edition*, Prentice Hall, Upper Saddle River, New Jersey, 1993
- [36] N. H. Balshaw, *Practical Cryogenics*, Published by Oxford Instruments Superconductivity Ltd. 2001
- [37] Oxford Instruments Superconductivity Ltd., *Spectromag Operator's Handbook*, 2005
- [38] B. E. A. Saleh, M. C. Teich, *Fundamentals of photonics*, John Wiley & Sons, Inc. 1991
- [39] Hamamatsu Photonics, *Photomultiplier Tubes*, product catalogue, 1994
- [40] P. Ekström, *Statistics and the Treatment of Experimental Data*, Division of Nuclear Physics, Lund University, 1996
- [41] W. A. Phillips, *Tunneling States in Amorphous Solids*, J. Low Temp. Phys., **7**, 351–360, 1972
- [42] A. Suárez, R. Silbey, *Low-temperature dynamics in glasses and the stochastic sudden-jump model*, Chem. Phys. Lett. **218**, 445–453, 1994



# Appendix A

## Pulse Sequences

Separate pulse sequence files were loaded from the computer for each excitation intensity and magnetic field strength to be examined. A typical sequence is as follows:

```
3 trigM1_300ns trigM1_300ns
2 wait1us wait1us
1 g800ns_0_25 Pulse350_2_5us
2 wait1us wait1us
1 wait1us wait1us
1 g800ns_1 Pulse350_2_5us
2 wait1us wait1us
3 wait300ns wait300ns
12 trigM2_300ns trigM2_300ns
1 wait1us wait1us
1 g800ns_1 Pulse350_2_5us
100 wait10us wait10us
500 erase200us sqr350_200us
2000 wait100us wait100us
1 g800ns_0_25 Pulse350_2_5us
5 wait1us wait1us
1 wait1us wait1us
1 g800ns_1 Pulse350_2_5us
5 wait1us wait1us
3 wait300ns wait300ns
12 trigM2_300ns trigM2_300ns
1 wait1us wait1us
1 g800ns_1 Pulse350_2_5us
100 wait10us wait10us
500 erase200us sqr350_200us
2000 wait100us wait100us
.
.
.
1 g800ns_0_25 Pulse350_2_5us
```

```

95 wait1us wait1us
1 wait1us wait1us
1 g800ns_1 Pulse350_2_5us
95 wait1us wait1us
3 wait300ns wait300ns
12 trigM2_300ns trigM2_300ns
1 wait1us wait1us
1 g800ns_1 Pulse350_2_5us
100 wait10us wait10us
500 erase200us sqr350_200us
2000 wait100us wait100us
1 g800ns_0_25 Pulse350_2_5us
98 wait1us wait1us
1 wait1us wait1us
1 g800ns_1 Pulse350_2_5us
98 wait1us wait1us
3 wait300ns wait300ns
12 trigM2_300ns trigM2_300ns
1 wait1us wait1us
1 g800ns_1 Pulse350_2_5us
100 wait10us wait10us
500 erase200us sqr350_200us
2000 wait100us wait100us
1 trig0 trig0

```

The instructions of the file are carried out sequentially, line by line. Each line is divided into three parts: A number, which tells how many times that line should be repeated, and two variable names, which describe what waveform should be output on the AWG channels 1 and 2 respectively. Only the output of channel 1 are of interest here; the channel 2 waveforms are a leftover from an earlier experimental setup. Since the file is repetitive and very large, only the beginning and the end of the file are shown.

The names `g800ns_0_25` and `800ns_1` denote gaussian shaped pulses with a full width half maximum (FWHM) of 800 ns and with a peak intensity of 0.25% and 1% of the maximum output power of the AOM. The `trigM1_300ns` and `trigM2_300ns` are sequences in which TTL signals are sent from the digital outputs M1 and M2 respectively. The `erase200us` is a pulse that scans a wide interval for 200  $\mu$ s. The various `wait` variable names are just used to create delays.

On the first line, a TTL signal is sent through one of the digital outputs of the AWG. This signal tells the oscilloscope to start to collect data. After that, two excitation pulses are sent out (commands `g800ns_0_25` and `g800ns_1`). When the echo is expected, a second TTL signal (`trigM2_300ns`) is sent out. This signal serves two purposes: It opens the gate to the photomultiplier tube, and it sends a trigger signal to the oscilloscope. After that, a third pulse, identical to the second excitation pulse, is sent. The purpose of this is to be used as a reference to be able to calculate how much light was absorbed in the crystal. The excitation pulses can not be used for this, as they move in relation to the trigger signal when the pulse separation time is changed. After a delay, the

erasing pulses (`erase200us`) are sent. After this, there is a 200 ms delay, after which a new excitation pulse sequence is sent out, with a longer pulse separation time. The sequence consists essentially of 33 subsequences that are identical in every way except for the pulse separation time, which grows with  $3 \mu\text{s}$  for each subsequence.

When the measurements were to be done, the oscilloscope was set up to collect a total of 660 measurement values, recording values from both the photomultiplier tube and the two photodiodes. The sequence described above was initiated in a repeat mode, which made the sequence described in the file run multiple times. After 20 runs, the oscilloscope had collected all its 660 values, which were then stored on disk.

The sequences for measuring the coherence times at other excitation densities were identical to the one shown above, but with different peak intensities of the excitation pulses.



## Appendix B

# Spectromag Operation

The aim of this chapter is to provide a detailed description of how to operate the Spectromag cryostat and to give descriptions of some problems that have been encountered, along with solutions. Note that this document is intended as a supplement to the manual, not as a substitute. In particular, it does not comprehensively cover safety issues.

### B.1 Overview

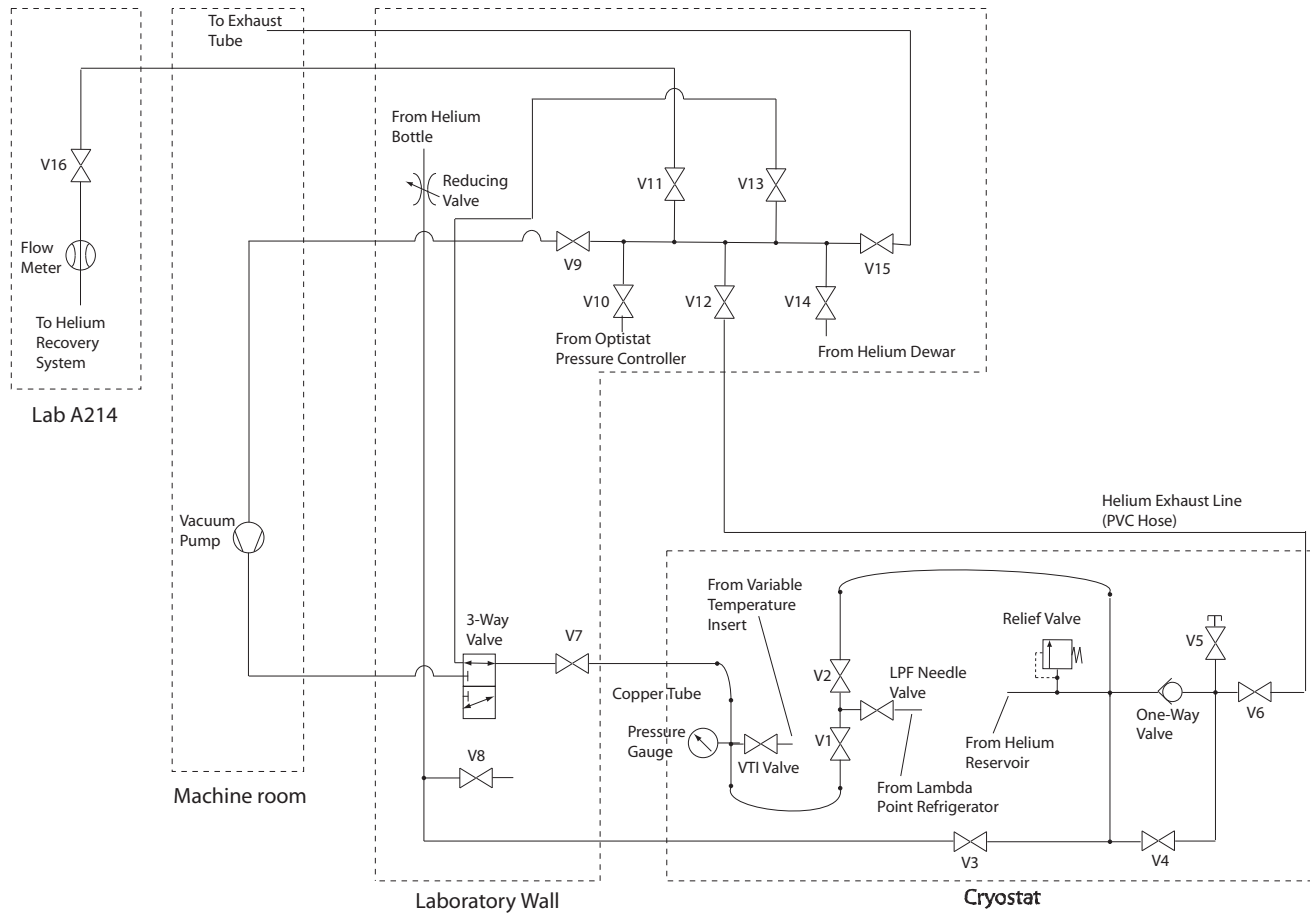
A general overview of the Spectromag has been given in chapter 5. Much information about the cryostat itself can also be found in the supplied manual [37]. However, the manual is very generic and does not contain explicit “how to” instructions. Also, the connections to the vacuum pump and the helium recovery system are specific for this particular laboratory, and are somewhat complex.

#### B.1.1 Hose Connections

The hoses and hose connections have several purposes:

- To pump the helium reservoir, the Lambda Point Refrigerator (LPF) and the Variable Temperature Insert (VTI) to vacuum as a part of the pump and flush procedure performed before cooling.
- To provide a supply of helium gas to the cryostat, used in the pump and flush procedure.
- To regulate the pressure of the LPF and VTI in order to control their temperature while they are running.
- To collect the helium that boils away and transfer it to the helium recovery system.

Figure B.1: Schematic of the external hose connections.



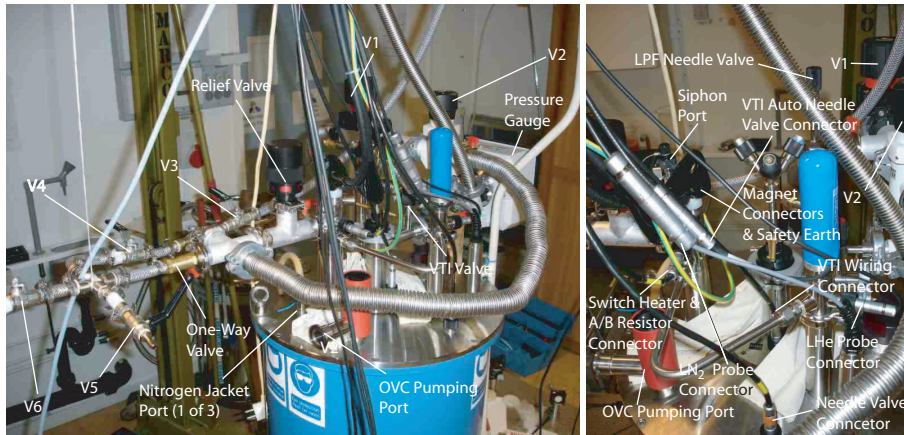


Figure B.2: *The top of the cryostat, with all valves and electrical connectors labelled.*

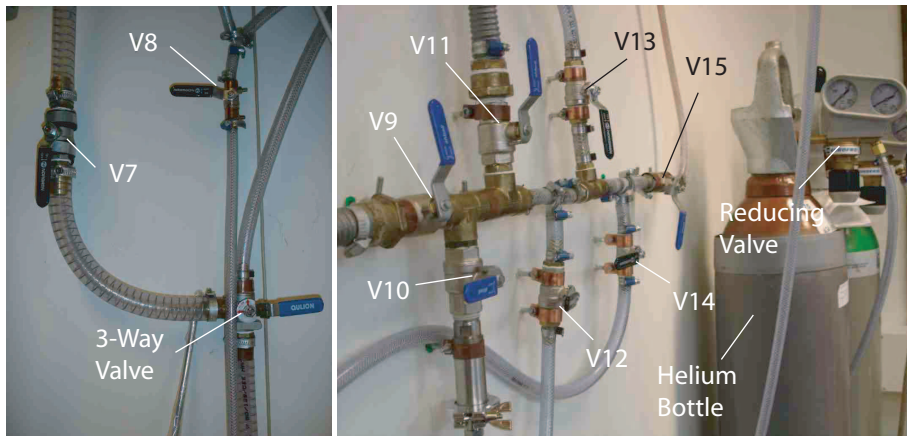


Figure B.3: *The valves mounted on the laboratory wall.*

A schematic of the hose connections is found in figure B.1. All valves have been labelled in order to facilitate the descriptions of how to operate the system. Figures B.2 and B.3 show how the connections look like in real life. The cryostat can be connected to the helium recovery in two ways: either through a copper tube connected through a flexible hose to the VTI, and from there to the rest of the cryostat, or through a PVC hose from valve V6. Only the copper tube is designed to handle a large amount of cold gas, and it must therefore be used when the cryostat is being cooled down or refilled. When the VTI or LPF is in operation, the copper tube is used to connect them to the vacuum pump, and in this case the PVC hose must be used to collect gas from the reservoir.

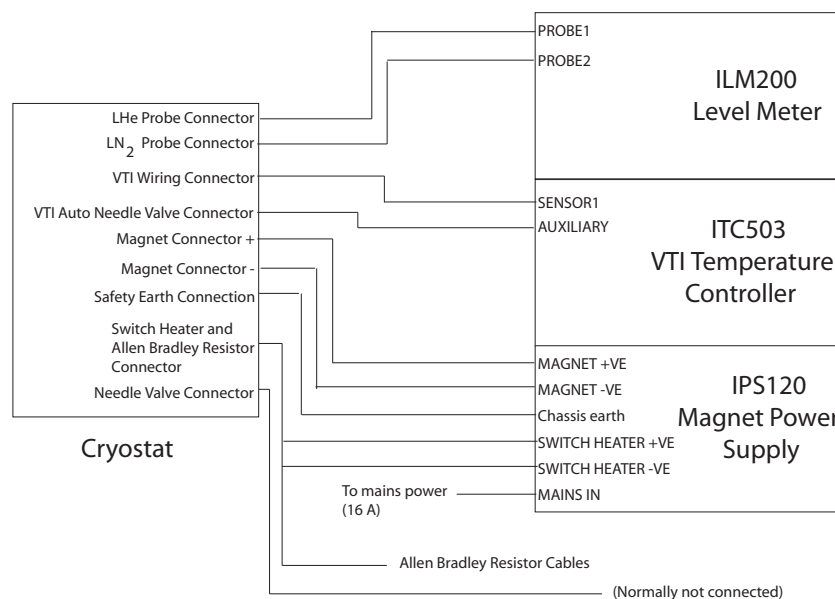


Figure B.4: *Schematic of the electrical connections between the cryostat and the control boxes. Connectors that are labelled in capital letters are labelled in the same way on the actual control boxes. The other labels are descriptive names.*

### B.1.2 Electronics

The cryostat is connected to an ILM200 level meter, an ITC503 temperature controller and an IPS120 magnet power supply. The connections are shown in figure B.4. Note that the connector called *Needle Valve Connector* is normally not connected to anything. In the event of ice blocking the VTI auto needle valve, the blockage can be cleared by applying current to this connector.

### B.1.3 Allen Bradley Resistors

The temperature in the helium reservoir is monitored using three *Allen Bradley resistors*. These are carbon resistors which have a very deterministic relationship between their resistance and their temperature, and they can therefore be used as thermometers. The relationship between resistance and temperature is inverse and very nonlinear; a higher resistance means a lower temperature, and a given temperature change gives a much greater resistance change at low temperatures than at higher ones.

The Spectromag is equipped with three Allen Bradley resistors, labelled R1, R2 and R3. R1 is mounted 10 cm above the LPF, R2 is on the LPF and R3 is on top of the magnet. Their values can be read by using the leads going in the same cable as the switch heater leads. To measure R1, connect a resistance meter to the green and the yellow cable. For R2, use the green and white cables, and for R3, use the green and black cables. Calibration values for the resistors can be found in the cryostat manual, in the *Specifications, wiring and test results*

section.

## B.2 Cooling the system

Cooling the system from scratch can take a long time. It is advisable to begin this procedure a few days before any planned experiments. The cooling procedure is as follows:

1. Pump the Outer Vacuum Chamber (OVC) to a high vacuum. This is done by connecting a suitable high vacuum pump to the OVC pumping port. The pump used by the group, a Leybold Vacuum PT 70F Compact turbomolecular pump containing both a forepump and a turbopump, has not a sufficiently high pumping speed for efficient operation, and it is usually necessary to switch the pump operation to manual mode and start pumping using only the forepump for at least a few hours, preferably over the night, until the pressure has dropped to a few mbar or less. After that, start the turbopump and let it pump until the pressure reaches around  $10^{-5} - 10^{-6}$  mbar. This can take a day. If the pressure has not been lowered sufficiently when the turbopump is engaged, the pump will overheat after a while and shut down to prevent damage. If so, it is necessary to pump the OVC to an even lower pressure using the forepump before the turbopump is started.

Continue to pump the OVC until the liquid helium transfer starts.

2. Pump and flush the helium reservoir. This is done to remove all air, and especially all water vapour, from the system. Any vapour left in the system could cause ice blockages of valves and capillary tubes when the system is cooled down. To pump the system, make sure that valves V1, V2, V7 and V9 are open, and that the 3-way valve is set to connect the cryostat to the vacuum pump. All other valves on the cryostat should be closed. Also, close V11 and open V15, so that the air in the cryostat is pumped to the exhaust rather than to the helium recovery system.

NOTE 1: When this is being written, the exhaust consists of a hose that has to be put out through a window when used. Hopefully, a more permanent solution will be made in the long run.

NOTE 2: If a dewar is connected to the helium recovery through V14, it should be disconnected when doing this part of the procedure.

Start the vacuum pump. When the pressure drops to less than 1 mbar (which it should almost immediately), close V7 to stop the pumping. Now, flood the reservoir with helium gas by opening the helium bottle, adjusting the reducing valve to 3/4 bar and opening valve V3. When the reservoir is back at atmospheric pressure, close V3.

3. Pump and flush the Lambda Point Refrigerator. To do this, close V2 and open V7. When the pressure has dropped below 1 mbar, close V7 and open the LPF needle valve. This will flush the LPF with helium gas from

the main reservoir. Close the LPF needle valve. Repeat this procedure a couple of times. Leave the LPF valve closed.

4. Pump and flush the Variable Temperature insert. For this, open the VTI valve, and pump it to vacuum by opening V7. Next, close V7 and fill the VTI with helium gas from the main reservoir by opening the VTI auto needle valve, which connects the VTI to the main reservoir. The needle valve can only be operated using the ITC503 control box. Press and hold the GAS FLOW button, and adjust the needle valve by using the RAISE and LOWER buttons. The display will show the position of the valve in percent (100% is fully open). When the pressure has risen to 1000 mbar, close the VTI auto needle valve. Repeat this procedure a couple of times. Leave the VTI auto needle valve closed.

NOTE 1: Beware of the difference between the *VTI valve* and the *VTI auto needle valve*. The former is a manually operated valve connecting the VTI to the pumping line. The latter is a motorized needle valve that connects the VTI to the helium reservoir and is operated using the ITC503 controller.

NOTE 2: Make sure that you do not put the auto needle valve in auto mode by mistake. This happens if the GAS FLOW button is pressed and released without the use of the RAISE or LOWER buttons, and causes the button light to light up. If this happens, disengage auto mode by pressing the button a second time.

5. Fill the main reservoir with liquid nitrogen in order to cool it to 77 K. To do this, insert the nitrogen transfer tube into the siphon port. Close V2 and open V4 and V5 to make sure that the nitrogen can vent. Now, fill the main reservoir from a nitrogen dewar. Typically, 50 liters are used to cool down and fill the reservoir, and the procedure takes approximately an hour. When the reservoir is full, put a piece of latex hose or something similar on the nitrogen transfer tube to make sure no water vapour can enter the cryostat that way. Leave the system for a few hours, or over the night, to make sure that all parts are completely cooled down.

NOTE 1: It is not easy to estimate the level of liquid nitrogen. The level meter in the main reservoir works only for liquid helium, and is of no help during this procedure. However, some information can be obtained by monitoring the Allen Bradley resistors. When the liquid level reaches a resistor, its reading will stabilize at the liquid nitrogen temperature value. It is also possible to just keep filling until liquid nitrogen can be seen coming from the exhaust port at V5.

NOTE 2: Occasionally, it has seemed that the efficiency of the transfer is hampered by the high resistance of the exhaust system (valves V4 and V5). This reduces the rate at which nitrogen gas can leave the reservoir and creates a high pressure in the system, opposing the transfer. It is possible to temporarily remove the flexible vacuum tube attaching the helium reservoir to the LPF to create a larger exhaust port and achieve higher transfer rates.

6. Transfer the liquid nitrogen from the main reservoir to the nitrogen jacket.

To do this, attach the top of the nitrogen transfer tube to a nitrogen jacket port with a piece of latex hose. Make sure that the helium bottle is open and that the reducing valve shows around 3/4 bar. Close V4 and V5 and apply pressure to the reservoir by opening V3. This should start to blow the nitrogen into the jacket. The nitrogen level meter should start to rise. After a while, the meter levels out and the sound from the transfer changes slightly. Now, V3 can be closed. Remove the nitrogen transfer tube from the siphon port and insert the siphon bung.

NOTE 1: The relief valve on the cryostat will open at rather low pressures. When blowing out the liquid nitrogen, care must be taken not to apply too much pressure from the helium bottle. If that happens, the relief valve will open to let out the excess gas, and a lot of helium will be wasted in this way. Use the V3 valve to regulate the gas flow such that the relief valve does not start to hiss.

NOTE 2: If the nitrogen jacket did not receive any significant amounts of nitrogen from the reservoir, fill it from a dewar at this point. The jacket must not be completely empty while liquid helium is being transferred. However, there has been a suggestion that it might not be a good idea to fill the jacket completely before the helium reservoir has been filled with liquid helium. The reason would be that there is a thermal connection between the reservoir and the jacket at the top of the cryostat, and this connection is removed when the metal responsible for the connection drops to superconducting temperatures. To be on the safe side, it might be advisable not to fill the jacket to more than 50 percent before the liquid helium transfer is complete.

7. Make sure that all the nitrogen has been removed from the helium reservoir. To do this, pump vacuum in the reservoir by opening V1, V2 and V7 and making sure that the vacuum pump is on. It is important that the nitrogen transfer tube has been removed and the siphon bung inserted when you do this. Otherwise, you will draw air, including water vapour, into the system. Monitor the Allen Bradley resistors. If the resistance increases, it is a sign that there is still liquid nitrogen left. Another test is to temporarily close V7. If the reading on the pressure gauge immediately starts to rise, the nitrogen has not been completely removed. If so, continue pumping until it is. If one wants to be absolutely sure that all nitrogen has been removed, it is possible to wait until the resistances of the Allen Bradley resistors have dropped below the 77 K values. However, it is usually necessary to wait a very long time for this to happen (several hours) and it should not be necessary.
8. Pump and flush the helium reservoir, LPF and VTI again in the same manner as in steps 2–4.
9. Connect the main reservoir to the helium recovery. To do this, make sure that valves V1, V2, V13, V11 and V16 are open and that the 3-way valve is set to connect the cryostat to valve V13. Also, close V15. Switch off the vacuum pump and then open V7. Note that it is important that the helium gas leaves the cryostat through the copper tube and not through the PVC hose connected to V6, as the latter is not designed to handle

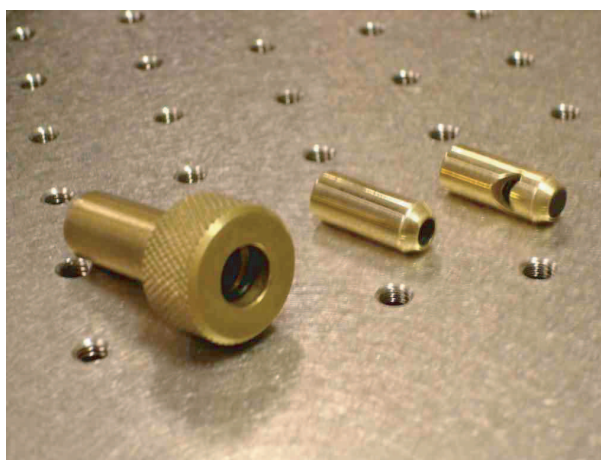


Figure B.5: *From left to right: The transfer tube adapter, the transfer tube mouthpiece intended for cooldown procedures, and the transfer tube mouthpiece intended for refilling procedures.*

such a large amount of cold gas. Because of this, make sure that V6 is closed.

10. Write down the reading of the return gas meter in the logbook.
11. Now the helium transfer can be started. Make sure that the right mouthpiece is attached to the cryostat leg of the transfer tube. It should be the one that lets the helium straight down (figure B.5). If the transfer tube used is of the rigid type, the helium dewar must be placed on a lift so that its vertical position can be adjusted. Attach the transfer tube adapter to the dewar and lower the transfer tube into it until helium gas starts to emerge at the other end. This should produce a clearly audible hissing sound. If necessary, pressurize the dewar with a rubber bladder.

Now, the other end of the tube can be inserted in the cryostat siphon port. Slowly lower the tube until its legs have reached the bottom of the cryostat and the dewar. The best way to control the transfer is to pressurize the dewar with helium gas. This can be done by connecting the dewar to the helium port at valve V8 with a latex rubber hose. Install a pressure regulator or a needle valve on this hose if it is not already installed, and make sure that it is initially closed. Open the valve on the helium bottle and valve V8 and set the reducing valve on the bottle to  $3/4$  bar. It is also advisable to connect a pressure meter to the dewar and the cryostat. A method that works is to attach the meter as in figure B.6. By opening and closing the valves, it is possible to switch readings between the cryostat and the dewar. Make sure that both valves are not open at the same time, as this would eliminate the pressure difference between the cryostat and the dewar, stopping the transfer. The pressure meter mounted on the dewar has been found to be unreliable and imprecise.

Now, adjust the pressure regulator or needle valve to keep a pressure difference between the dewar and the cryostat of 10–15 mbar. Close the

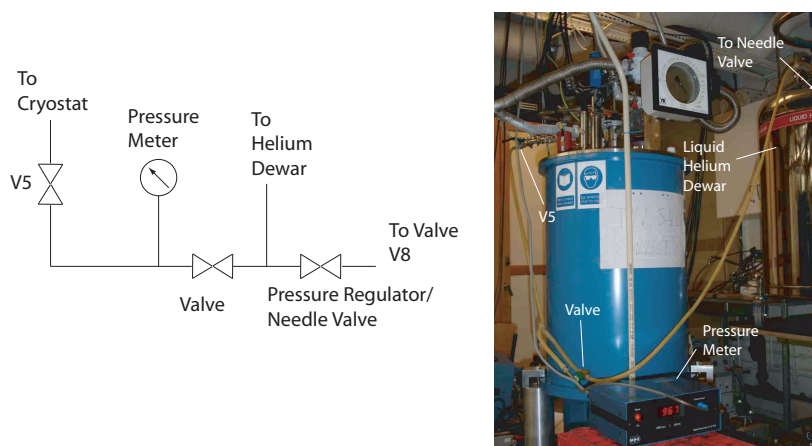


Figure B.6: *Connections used to pressurize the dewar and to monitor the pressure in the dewar and the cryostat. The pressure regulator/needle valve is used to control the pressure in the dewar. The other two valves are used to select what pressure the meter should monitor. It is important that these two valves are not open at the same time. Disregard the note on the cryostat.*

OVC pumping port, as the OVC should now get cryopumped to a pressure below that of the pump, so the pump would now actually introduce more gas than it pumps away. From this on, the turbopump does not need to be used as long as the cryostat is at liquid helium temperature. Also monitor the recovery line; it should be covered with ice for at most two meters length. Periodically check the gas flow on the return gas meter in laboratory A214. Normally, the rate should be ten liters of gas in 5–12 seconds, which corresponds to 4–10 liters of liquid per hour. Check the Allen Bradley resistors regularly — their values should initially rise by approximately 1–2  $\Omega$  every five minutes.

NOTE 1: It is advisable not to measure the resistance of the Allen Bradley resistors continually, as this will introduce heat to the system, although it is not clear how much effect this has. It should suffice to switch on the resistance meter temporarily every five or ten minutes.

NOTE 2: It is extremely important that the transfer tube provides proper heat isolation. Helium has an extremely low latent heat of evaporation, and bad isolation can cause much of the helium to boil even before it has reached the cryostat. Check that the tube is at room temperature on the outside along its whole length. A couple of cold spots on the tube may be acceptable, but not much more.

Cooling down typically takes one hour. You can see that liquid starts to collect when the Allen Bradley resistors stabilize around their 4.2 K resistance values, and the ice on the recovery line starts to melt. Set the He level meter to FAST mode, which means it measures the level every twenty second rather than once an hour, and increase the differential pressure between the dewar and the cryostat to 30–50 mbar. The reading on the level meter will typically rise quickly to 30–40%. After that, the

level should rise with on average 1% every twenty seconds or better.

When the level meter has reached 100%, remove the transfer tube from both the cryostat and the dewar. Insert the siphon bung in the siphon port.

12. Connect the dewar to the helium recovery system, remove the hoses used for pressurization and pressure measurement, and close all valves in the helium bottle line. Set the level meter to SLOW readings.
13. Write down the reading of the return gas meter in the logbook. Typically, the meters shows that 10–15 liters of liquid ( $\approx 7\text{--}10\text{ m}^3$  of gas) have been consumed during the procedure.

## B.3 Operating the system

### B.3.1 Operating the magnets

The magnet is equipped with a superconducting switch, which makes it possible to run the magnet in *persistent mode*. In this mode, the current is going through a closed superconducting loop, and since such a loop has no resistance, it can hold the current for a very long time without any need to apply a voltage across the magnet coil. See the schematic in figure B.7. The main benefit of persistent mode when it comes to this cryostat is that in this mode there is no current in the magnet leads, which reduces the helium boil-off rate. The switch is made

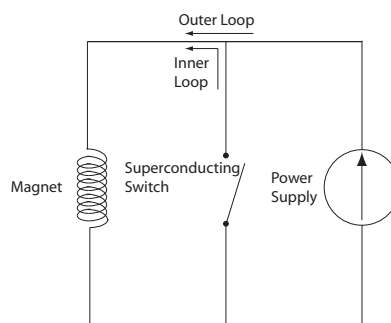


Figure B.7: *Simplified schematic of the magnet circuit. When the superconducting switch is open, the outer loop is used, and the current output of the power supply controls the current in the magnet. When the switch is closed, the inner loop is used, and the current in the leads from the power supply does not affect the magnet. The magnet is now in persistent mode, and the power supply current can be reduced to zero without turning off the magnetic field. In reality, there is also a protection circuit wired in parallel with the magnet.*

of superconducting material, and is operated by a small heater. It is opened by turning the heater on. This heats the switch to a normal (non-superconducting) state. Its resistance in this state is only a few  $\Omega$ , but this is sufficient to make

essentially no current go through it. To close the switch, the heater is turned off, which makes the switch superconducting.

When the magnet power supply is first turned on, the button HOLD must be pressed to release the supply from its initial, clamped state. To change the magnetic field, turn on the switch heater and wait approximately 30 seconds to make sure the switch is open. Now, set the sweep rate and the field strength by pressing and holding the SET RATE and SET POINT respectively and using the RAISE and LOWER buttons. Use the CURRENT/FIELD button to select whether the display should show current or magnetic field. The polarity can be set by pressing the CHANGE POLARITY button while the SET POINT button is being depressed. When all parameters are set, press GOTO SET, and the magnet will be swept to the desired field.

NOTE: It is important not to sweep the field too fast. Recommended energization rates can be found in the *Specifications, wiring and test results* section of the cryostat manual.

When the magnet has reached the desired field, it can be put in persistent mode. To do this, turn off the switch heater by pressing the SWITCH HEATER button and wait for 30 seconds. Now, press GOTO ZERO to sweep down the current in the magnet leads to zero. The PERSISTENT MODE light should light up. To turn off persistent mode, change the current in the magnet leads so that it matches the current in the magnet, and turn on the switch heater. It is very important that the current is the same in the leads as in the magnet when the switch heater is turned on, and because of this, the power supply has an interlock that prevents the user from turning on the heater if there is a mismatch. If necessary, this interlock can be overridden by holding down the SWITCH HEATER button for four seconds.

Both the magnet field and the power supply output voltage must read zero before the power supply is turned off.

### B.3.2 Operating the VTI

The cryostat has been operated at temperatures below 4.2 K using either liquid helium or helium gas. In both cases, the idea is to supply helium from the main reservoir through a capillary tube, and to use a vacuum pump to control the vapour pressure, and thus the temperature, in the VTI.

To cool using liquid helium, close valves V1 and/or V2 and make sure V9 is open. Also, open V6 and V12, so that there is a path to the recovery system for helium boiling off from the main reservoir. Partly open the VTI auto needle valve to a position of 25–30% by pressing and holding the GAS FLOW button and using the RAISE and LOWER buttons on the ITC503. This will let helium from the main reservoir into the VTI. Wait until the temperature indicated on the ITC503 has dropped to 4.2 K, and wait a while longer so liquid helium can collect in the VTI. Now, reduce the auto needle valve setting to 17–20% and start to pump on the VTI by starting the vacuum pump, setting the 3-way valve to connect the cryostat to the pump and partly opening V7. By adjusting the position of V7 it is possible to quite accurately adjust the temperature of the

VTI to the desired value. In this regime, the sample is immersed in liquid, and the pump is used to reduce the vapour pressure above the liquid. Note that when performing experiments with the sample in liquid helium, it is necessary to use temperatures below 2.17 K, where  $^4\text{He}$  becomes superfluid. Above this temperature, bubbles in the helium will scatter laser beams in unpredictable ways.

If the temperature suddenly starts to rise, the VTI auto needle valve setting has probably not been sufficiently open, which has depleted the VTI of helium. Open the VTI auto needle valve to 25–30% to refill the VTI, and then continue to operate the cryostat with the auto needle valve in a slightly more opened position than previously.

To operate in gaseous helium, start to pump the VTI already before it has reached 4.2 K. In this regime, liquid will never collect. Instead, helium entering the VTI will immediately evaporate, and the cold gases will cool the sample. In this way, temperatures above 2.17 K can be used, but the cooling power provided to the sample is probably less. When doing experiments with intense laser light with long duration, liquid helium might thus be a better alternative.

It is also possible to operate the VTI at temperatures up to 300 K by using a built-in heater, but this has not been tried. Refer to the manual for details about this.

### B.3.3 Operating the LPF

This has not been tried. Refer to the manual for details about this. Note, however, that in the present hose connection configuration, it is not possible to control the pressure of the VTI and the LPF independently of each other. It is possible that the connection scheme needs to be revised if the LPF is to be used.

## B.4 Refilling the system

When refilling the system, the *phase separator* mouthpiece (figure B.5) should be used. The idea with this mouthpiece is that warm helium gas will be directed upwards, away from the liquid level, while the heavier cold liquid will fall down. This reduces the risk of the helium already in the cryostat boiling away as a result of heat introduced by warm gas.

Use the helium transfer procedure described in section B.2, steps 10–13. However, it is advisable not to lower the transfer tube below the liquid level in the cryostat. Use the level meter on the ILM200 to try to estimate where this is. A tube that is not properly pre-cooled could cause a significant boil-off if it was lowered into the liquid. Also, immediately switch the level meter to FAST mode when the transfer is begun.

## B.5 Encountered Problems

### B.5.1 Wrong mouthpiece

In the initial test run, the phase separator mouthpiece was used during cooldown, due to insufficient information in the manual. This is unacceptable: The helium must be delivered to the very bottom of the cryostat. However, this was not the only reason for the failure; see the next subsection.

### B.5.2 Faulty Transfer Tube

In the initial attempts to cool the system down, the temperature initially dropped as expected. However, it could not be lowered all the way down to 4.2 K, but stopped at approximately 15 K. By applying an extremely high pressure in the dewar, the temperature could be lowered almost to liquid helium temperature, but no liquid would collect. After several attempts, it was discovered that the transfer tube had a major leak, which caused its vacuum space to have a far too high pressure. As a consequence, a substantial amount of heat was introduced into the helium on its way to the cryostat, which caused it to evaporate completely before it had reached the cryostat, even at very high transfer rates. It was noted that the legs of the tube were cold enough to make water condense. A valuable lesson was that due to the extremely low latent heat of evaporation of helium, the transfer tube must be extremely well isolated.

### B.5.3 Long Extension Pieces

In the subsequent attempts, another transfer tube with superior performance was used. Even so, liquid would only collect to 30–50%, despite several efforts to fill it further. An inspection of the transfer tube showed that the heat isolation worked as it should. Eventually, it was found that an extension tube, attached to the dewar leg of the transfer tube to make it easier to reach the bottom of the dewar, was the cause of these problems. The extension tube is not isolated in any way, but should not cause any problems if it is short, as the temperature immediately above the liquid surface is 4.2 K. In this case, when the liquid level in the dewar dropped below a certain level, a too large part of the unisolated extension tube was above the surface (approximately 30 cm). At this point, the introduced heat caused all liquid to evaporate before it had reached the cryostat. This explains why the cryostat stopped collecting liquid at a certain point. The lesson is to avoid extension tubes if possible, and if not possible, to use as short extension tubes as possible.

### B.5.4 Bent Brass Tube

When the cryostat was tested, it was noted that the helium evaporation rate was much higher than specified, while the nitrogen evaporation rate was much lower than specified. The obvious explanation was that there was some unwanted

thermal connection between the nitrogen cooled part and the helium cooled part. Inspection showed that the culprit was a brass tube, which is attached at its bottom to the nitrogen cooled shield and encloses the VTI. The tube is cooled to 77 K by the nitrogen shield and is supposed to work as a radiation shield between the magnets and the VTI, since the VTI is designed to operate at any temperature up to 300 K, while the magnets always operate at a temperature of 4.2 K or lower. When the cryostat was installed, the bottom part of it was temporarily removed to remove packing pieces. When the cryostat is reassembled, you are supposed to remove a brass plate which is attached to the nitrogen cooled shield tail, and which fits into the brass tube. The brass plate is reattached after the shield tail has been reassembled. However, due to lack of information, this had not been done during the installation, and as a result, the brass tube had been bent and had contact with the helium reservoir. To repair this, the brass tube had to be removed from the cryostat. To remove the tube, it is necessary to lift the cryostat on a hoist, and then to remove its lower part along with the radiation shield tail, so that the coil-shaped magnet compartment is visible. Now, the VTI must be separated from the capillary tube connecting it to the main reservoir. The capillary tube is fitted on the underside of the VTI with three screws and sealed with indium. These screws must be unscrewed, and a “jacking screw” inserted in a fourth hole on the underside of the VTI to force the VTI and capillary tube apart. The VTI is attached to the small top plate of the cryostat through a tube. By unscrewing the small top plate and lifting it straight up, the VTI can now be removed. The brass tube can then be removed by pulling it straight up. It turned out to be possible to straighten it using a brass cylinder and a hammer. The reassembly procedure is essentially the same as the removal procedure in reverse. Note that the old indium must be removed from the seal by for example a sharp knife, and a piece of fresh indium wire put in its place. Figure B.8 clarifies some details.

### B.5.5 Nitrogen Level Probe Malfunction

A minor problem, but still worth to mention. When the cryostat is returned to room temperature after having been cooled down, the nitrogen level meter begins to show erroneous readings. The reason is believed to be that when the cryostat is cold, water will enter the open nitrogen jacket ports and condense to ice. When the cryostat is returned to room temperature, the ice will thaw and contaminate the level probe. The probe consists of two concentric metal cylinders and measures the capacitance between these. The scheme utilizes the fact that the dielectric constant for liquid nitrogen is significantly higher than for gaseous nitrogen. However, water has a very high dielectric constant and will cause the reading to go off the scale. The solution is to remove the probe and keep it in a dry place until all water has evaporated. See figure B.9 for instructions of how to remove the probe.



Figure B.8: *Repairing the bent brass tube. (a) The author working on the capillary tube. (b) The underside of the VTI after the capillary tube has been removed. The three ordinary screw holes and the “jacking screw” hole are clearly visible. (c) The VTI has now been removed. The brass tube is unscrewed from above, and is removed by lifting it straight up. (d) A solid brass cylinder, custom-made to fit the tube exactly, is inserted into the tube, and the tube is carefully cold forged with a hammer until it is completely straight. The picture shows Brian Julsgaard (top) and Lars Rippe at work.*



Figure B.9: *The nitrogen probe. To remove it, first disconnect its connector to the level meter. After that, unscrew it at the point indicated and lift it straight up.*